A&A 555, A71 (2013)
DOI: 10.1051/0004-6361/201321444

Astronomy & Astrophysics

The *Herschel* Gould Belt Survey in Chamaeleon II

Properties of cold dust in disks around young stellar objects⋆,⋆⋆

L. Spezzi[1], N. L. J. Cox[2], T. Prusti[3], B. Merín[4], Á. Ribas[4], C. Alves de Oliveira[5], E. Winston[3], Á. Kóspál[3], P. Royer[2], R. Vavrek[4], Ph. André[6], G. L. Pilbratt[3], L. Testi[1], E. Bressert[7], L. Ricci[8], A. Men'shchikov[7], and V. Könyves[6]

[1] European Southern Observatory, Karl-Schwarzschild-Strasse 2, 85748 Garching bei München, Germany
e-mail: lspezzi@eso.org
[2] Instituut voor Sterrenkunde, KU Leuven, Celestijnenlaan 200D, 3001 Leuven, Belgium
[3] Research and Scientifc Support Department, European Space Agency (ESA-ESTEC), PO Box 299, 2200 AG Noordwijk, The Netherlands
[4] *Herschel* Science Centre, European Space Astronomy Centre (ESA), PO Box, 78, 28691 Villanueva de la Cañada, Madrid, Spain
[5] European Space Astronomy Centre (ESA), PO Box, 78, 28691 Villanueva de la Cañada, Madrid, Spain
[6] Laboratoire AIM, CEA/DSM – CNRS – Universit Paris Diderot, IRFU/SAp, CEA Saclay, 91191 Gif-sur-Yvette, France
[7] CSIRO, North Ryde NSW 2113, Australia
[8] Division of Physics, Mathematics and Astronomy, California Institute of Technology, MC 249-17, Pasadena, CA 91125, USA

Received 11 March 2013 / Accepted 17 May 2013

ABSTRACT

Context. We report on the *Herschel* Gould Belt survey (HGBS) of the Chamaeleon II (Cha II) star-forming region, focusing on the detection of Class I to III young stellar objects (YSOs).
Aims. We aim at characterizing the circumstellar material around these YSOs and at understanding which disk parameters are most likely constrained by the new HGBS data, which are expected to be crucial for studying the transition from optically thick disks to evolved debris-type disks.
Methods. We recovered 29 of the 63 known YSOs in Cha II with a detection in at least one of the PACS/SPIRE pass-bands: 3 Class I YSOs (i.e.,100%), 1 flat source (i.e., 50%), 21 Class II objects (i.e., 55%), 3 Class III objects (i.e, 16%), and the unclassified far-infrared source IRAS 12522-7640. We explored PACS/SPIRE colors of this sample and modeled their spectral energy distributions (SEDs) from the optical to *Herschel*'s wavelengths with the RADMC-2D radiative transfer code.
Results. We find that YSO colors are typically confined to the following ranges: $-0.7 \lesssim \log(F_{70}/F_{160}) \lesssim 0.5$, $-0.5 \lesssim \log(F_{160}/F_{250}) \lesssim 0.6$, $0.05 \lesssim \log(F_{250}/F_{350}) \lesssim 0.25$ and $-0.1 \lesssim \log(F_{350}/F_{500}) \lesssim 0.5$. These color ranges are expected to be only marginally contaminated by extragalactic sources and field stars and, hence, provide a useful YSO selection tool when applied together. We were able to model the SED of 26 of the 29 detected YSOs. We discuss the degeneracy/limitations of our SED fitting results and adopted the Bayesian method to estimate the probability of different values for the derived disk parameters. The Cha II YSOs present typical disk inner radii $\lesssim$0.1 AU, as previously estimated in the literature on the basis of *Spitzer* data. Our probability analysis shows that, thanks to the new *Herschel* data, the lower limits to the disk mass ($M_{\rm disk}$) and characteristic radius ($R_{\rm C}$) are well constrained, while the flaring angle ($1 + \phi$) is only marginally constrained. The lower limit to $R_{\rm C}$ is typically around 50 AU. The lower limits to $M_{\rm disk}$ are proportional to the stellar masses with a typical 0.3% ratio, i.e., in the range estimated in the literature for young Class II stars and brown dwarfs across a broad range of stellar masses. The estimated flaring angles, although very uncertain, point toward very flat disks ($1 + \phi \lesssim 1.2$), as found for low-mass M-type YSO samples in other star-forming regions. Thus, our results support the idea that disk properties show a dependence on stellar properties.

Key words. stars: pre-main sequence – ISM: clouds – infrared: stars – protoplanetary disks – instrumentation: miscellaneous – ISM: individual objects: Chamaeleon II

1. Introduction

Chamaeleon II (Cha II) is a low-mass star-forming region located in the Chameleon-Musca complex (see Luhman 2008, for a recent review). Because of its proximity (178 ± 18 pc; Whittet et al. 1997), young age (4 ± 2 Myr; Spezzi et al. 2008), and compact structure (it extends over less than ∼3 deg^2 in the sky), it has been the target of several multi-wavelength studies over the last ∼25 years. The credit for the observational exploration of the young stellar population of Cha II goes to many authors, and a detailed summary of these studies is given in Sect. 2.1 in Spezzi et al. (2008). Starting from 1977, early objective-prism Hα surveys identified the first T Tauri stars in the region. Subsequently, near- to mid-infrared (IR) studies reported embedded Class I and II sources, and ROSAT X-ray observations revealed a number of weak T Tauri stars. More recently, deep optical to mid-IR imaging and follow-up spectroscopy observations provided a complete census and characterization of the young stellar population in this region down to the brown dwarf regime. In 2003, Cha II was chosen as one of the targets of the *Spitzer* Space Telescope Legacy Program "From Molecular Cores to

⋆ *Herschel* is an ESA space observatory with science instruments provided by European-led Principal Investigator consortia and with important participation from NASA.
⋆⋆ Tables 2 and 3 are available in electronic form at http://www.aanda.org

Planet-forming Disk" (c2d; Evans et al. 2003), and these data allowed us to explore, for the first time, the properties of circumstellar disks around the young stellar objects (YSOs) in Cha II. The general results of this survey (Alcalá et al. 2008, and reference therein) show that the disk fraction in Cha II (70–80%) is exceptionally high compared with other star formation regions of similar age. Several of these YSOs show significant mass accretion, and Biazzo et al. (2012) determined their mass accretion rates.

Altogether, these studies make Cha II one of the best studied nearby star-forming regions, and our knowledge of its population is similar to that of other well-studied nearby star-forming regions, such as Taurus and Orion. For this reason, Cha II has been included in the *Herschel* Gould Belt survey (HGBS[1]) key project (André et al. 2010). The ultimate goal of the HGBS is to elucidate the formation mechanisms of prestellar cores out of the diffuse medium, which is crucial for understanding the origin of the distribution of stellar masses through the observations of cloud filaments, prestellar condensations, and Class 0 protostars. These questions will be addressed, for the specific case of the Chamaleon complex, in Alves de Oliveira et al. (in prep.). Additionally, data from the HGBS can be exploited to study the far-IR and sub-millimeter (sub-mm) emission from more evolved Class I to III YSOs. These data are expected to greatly improve the determination of circumstellar disk parameters such as disk mass and degree of flaring (Harvey et al. 2012b), which are crucial for understanding the multifaceted and still unclear transition from the optically thick disks to the evolved debris-type disks, and the associated planet-forming process (see Williams & Cieza 2011, for a recent review).

In this paper, we focus on the PACS/SPIRE detections and statistics of Class I to III YSOs in Cha II. Our aim is to characterize the circumstellar material around these YSOs and to understand which disk parameters are reliably constrained using the new HGBS data. This statistical approach is of paramount importance to fully exploit *Herschel* capabilities in the characterization of disks around T Tauri stars, because most of the work published so far focused on single objects (e.g., Cieza et al. 2011; Harvey et al. 2012a). The only exception is the paper by Harvey et al. (2012b), which analyzed PACS-only data for a sample of ∼50 very low-mass stars and brown dwarfs and, hence, it is biased to lower stellar masses than the sample presented here. This paper is structured as follows: in Sect. 2 we describe the observations and data reduction procedure. In Sect. 3 we analyze the YSO sample detected with the HGBS in Cha II. In Sect. 4 we explore the locus of YSOs in SPIRE/PACS color–color diagrams, and in Sect. 5 we determine relevant disk parameters for our sample through spectral energy distribution (SED) modeling. Finally, in Sect. 6 we summarize our results and draw our conclusions.

2. Observations and data reduction

The Cha II dark cloud was observed with the *Herschel* Space Observatory (Pilbratt et al. 2010) within the frame of the HGBS (André et al. 2010). The observations (Obs. ID 1342213180 and 1342213181) were conducted on 22–23 January 2011 in parallel mode using both PACS (Photodetector Array Camera and Spectrometer; Poglitsch et al. 2010) and SPIRE (Spectral and Photometric Imaging REceiver; Griffin et al. 2010). An area of 3.5 deg^2, centered at RA = $12^h58^m10^s$ and Dec = $-77^d28'28''$, was covered with PACS at 70 and 160 μm and with SPIRE at 250, 350 and 500 μm with a scanning speed of 60″/s. Additionally, PACS-only maps at 100 μm were obtained on 15 January 2011 (Obs. ID 1342212708, 1342212709) with a scanning speed of 20″/s, covering a smaller region of about 2.4 deg^2 (Fig. 1). The total observing time was ∼12 h, 6 h for the parallel mode and 6 h for the PACS-100 μm images. The observing strategy is described in more detail in André et al. (2010).

PACS data were reduced using the Scanamorphos map-making software (version 10; Roussel 2012). For SPIRE observations we used the *naiveMap* and *destriper* algorithms within HIPE (*Herschel* Interactive Programming Environment, version 9; Ott 2010). The full-width at half-maximum of the point spread functions (PSFs) indicates that the spatial resolution of our maps is 6″, 9″, 12″, 20″, 25″, and 36″ at 70, 100, 160, 250, 350, and 500 μm, respectively. We note that the PSF is slightly elongated in parallel fast-scan speed mode (Lutz 2010).

We visually inspected each map to check the detection of the known YSOs in Cha II (see Sect. 3), using their coordinates as provided in Spezzi et al. (2008). For the clearly detected YSOs, the photometry (Table 2) was recovered from the point-source catalog extracted from the PACS/SPIRE maps using the multi-wavelength source extraction algorithm *getsources* (Men'shchikov et al. 2012, version 1.121206); we adopted a searching radius of 15″, corresponding to three times the typical FWHM of the sources in our PACS-70 μm map, and visually checked the accuracy of the match for each YSO. An aperture correction is applied to the fluxes extracted with *getsources*, taking into account the aperture radii recommended for each *Herschel* band, i.e., 12″ for 70 and 100 μm, 22″ for 160 and 250 μm, 30″ for 350 μm, and 42″ for 500 μm (see the PACS point-source flux calibration technical note from April 2011, and Sect. 5.7.1.2 of the SPIRE data reduction guide). No color correction was applied. When no source was detected, we computed a flux upper limit (Table 3) as in Ribas et al. (2013), i.e., calculating the rms of the sky emission over 100 apertures taken around the source, using the coordinates provided in Spezzi et al. (2008) and the same aperture radii and correction factors as for detected sources.

Using the multi-wavelength catalog extracted with *getsources*, we also estimated that the 5σ detection limit for point-like sources of our maps is ∼150 mJy at 70 and 100 μm and ∼300 mJy at 160, 250, 350, and 500 μm (Fig. 2).

3. Statistics and fluxes of known YSOs in Cha II detected with *Herschel*

The most complete census of YSOs in Cha II up to date has been presented in Alcalá et al. (2008) and Spezzi et al. (2008). The Cha II young population consists of 63 objects. Their Lada classification (Lada & Wilking 1984) is as follows: no Class 0 objects, 3 Class I objects, 2 flat-spectrum sources, 38 Class II objects, 19 Class III objects, and IRAS 12522-7640, a far-IR source not classified because of the lack of near-IR data. We note that classification provided in Alcalá et al. (2008) is based on the SED slope (α) of the line joining the flux measurements at 2.2 μm (K-band) and MIPS-24 μm, and the Lada class separation as extended in Greene et al. (1994), i.e., $\alpha \geq 0.3$ for Class I, $-0.3 \leq \alpha < 0.3$ for flat-spectrum sources, $-1.6 \leq \alpha < -0.3$ for Class II sources, and $\alpha < -1.6$ for Class III sources.

On the basis of our visual inspection of the PACS/SPIRE maps, we found that the HGBS observations detected 29 out of 63 known YSOs in at least one of the six pass-bands: 3 Class I

[1] http://gouldbelt-herschel.cea.fr

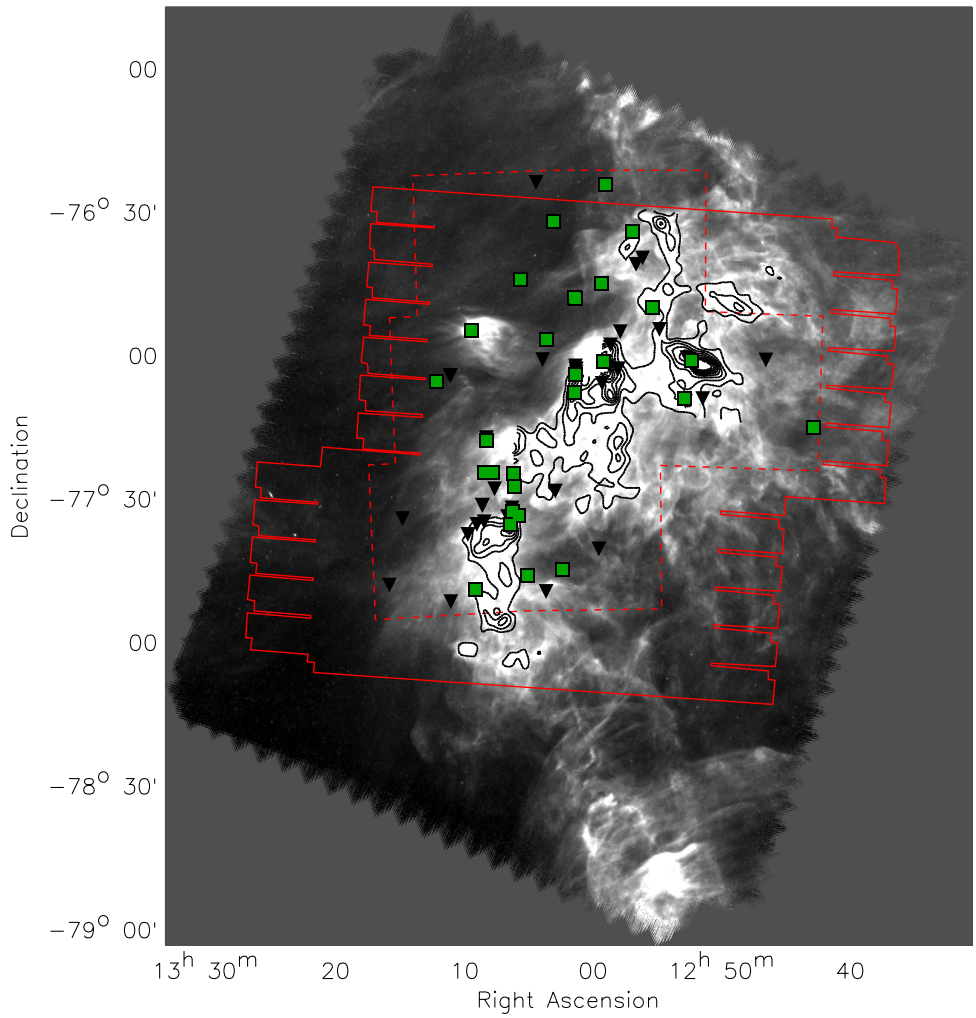

Fig. 1. SPIRE-250 μm map of Cha II. The continuous and dashed lines highlight the areas previously mapped in the infrared with *Spitzer* (Alcalá et al. 2008) and in the optical with ESO-2.2.m/WFI (Spezzi et al. 2007), respectively. The squares are the YSOs detected with the HGBS (Table 2). The triangles indicate the position of previously known YSOs not detected with the HGBS (Table 3). The contours from the *Spitzer*/IRAC extinction map (Alcalá et al. 2008) are also shown.

YSOs (100% of the previously known Class I sources), 1 flat-spectrum source (50% of the previously known flat-spectrum sources), 21 Class II objects (55% of the previously known Class II population), 3 Class III object (16% of the previously known Class III population), and IRAS 12522-7640. Table 1 summarizes the statistics of HGBS YSO detections in Cha II. In Table 2 we report the PACS and SPIRE fluxes for these 29 objects, together with their spectra type, Lada class, HGBS coordinates, and the distance between the HGBS coordinates and the coordinates reported in Spezzi et al. (2008) and Alcalá et al. (2008); we note that this distance varies from a few to a few-tenth arcsec, in agreement with the spatial resolution of the HGBS maps (Sect. 2).

For the sake of completeness, we report in Table 3 the flux upper limits in each band for the 34 undetected YSOs. We cannot add new information on these sources and, hence, do not treat them further in this paper. However, we notice that the estimated upper limits are consistent with the Lada classification and the SEDs presented for these objects in Alcalá et al. (2008).

As an additional check of our data reduction and flux extraction procedures, we also compared the 70 μm-flux of the detected YSOs as measured with PACS with the flux measured at the same wavelength with *Spitzer*/MIPS (Alcalá et al. 2008). In Fig. 3 we show the ratios of the PACS and MIPS fluxes at 70 μm as a function of the PACS fluxes. We find a typical value of 1.18 for this ratio and an rms of 0.24, meaning that there is no significant shift between the two datasets. Considering the uncertainties on PACS and MIPS flux measurements, the only clear outlier is IRAS 12496-7650, for which the PACS-70 μm flux is almost three times higher than that of MIPS-70 μm; we visually inspected this source in the PACS/MIPS mosaics and found out that its MIPS-70 μm flux (36.5 Jy; Alcalá et al. 2008) is slightly above the saturation limit of the MIPS mosaic, where saturation for point-like sources in low backgrounds occurs around 23 Jy (Evans 2007).

Moreover, Fig. 3 shows that our PACS observations basically detected all YSOs with a flux density higher than ~100 mJy in MIPS-70 μm. This value is slightly lower than the 5σ detection limit of our PACS-70 μm photometry (Sect. 2).

4. Exploring the YSO locus in PACS/SPIRE color–color diagrams

Infrared color–color (CC) diagrams are traditional diagnostic tools for investigating circumstellar matter around YSOs (Hartmann et al. 2005; Lada et al. 2006, and references therein).

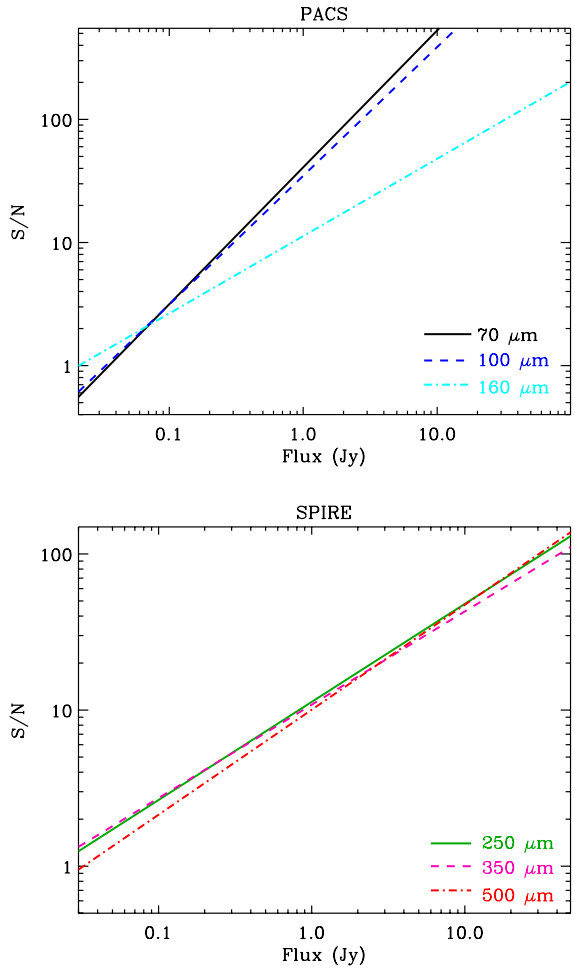

Fig. 2. Signal-to-noise ratio as a function of flux for point-like sources in our PACS (*upper panel*) and SPIRE (*lower panel*) maps as computed with *getsources* (version 1.121206) in the flux range covered by the Cha II YSOs.

Table 1. Statistics of Class I to III YSOs detected with the HGBS in Cha II.

Lada Class	N. of detections
I	3 (100%)
Flat	1 (50%)
II	21 (55%)
III	3 (16%)
Unknown	1 (100%)

Notes. We report between brackets the percentage of detections with respect to the total number of known YSOs in the given class.

However, the identification/classification of YSOs on the basis of mid- to far-IR colors is not trivial because of the high level of contamination (Sect. 3.1 in Evans et al. 2009; Harvey et al. 2007; Oliveira et al. 2009). Indeed, YSO colors in this wavelength regime are very similar to those of many background galaxies and, to a lesser extent, may also be mimicked by highly reddened stellar photospheres of older field stars. Harvey et al. (2007) provided a YSO selection tool on the basis of *Spitzer* IRAC/MIPS colors. By using *Spitzer* observations of the Serpens star forming-region and the SWIRE catalog of extragalactic sources (Lonsdale et al. 2003), these authors defined the boundaries of the YSO locus in several IRAC/MIPS color–magnitude and CC diagrams. Their criteria have proven to provide the best

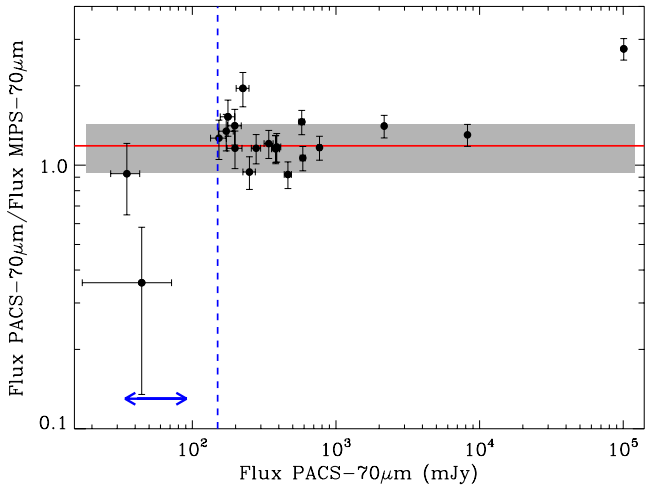

Fig. 3. Comparison between the flux at 70 μm as measured with PACS and the flux measured with MIPS at the same wavelength for the 23 YSOs in Cha II detected with the HGBS. The solid line and shaded area indicate the median value and the rms of the flux ratio, respectively. The arrow-head line displays the MIPS-70 μm flux range of Cha II YSOs not detected with PACS. The dashed line indicates the PACS-70 μm 5σ detection limit. The clear outlier is Sz 49, the faintest YSO detected with PACS.

separation between young stars and galaxies, with the fraction of remaining contaminants estimated to be around 30% (e.g., Spezzi et al. 2008; Oliveira et al. 2009; Cieza et al. 2010), and have been applied to select YSO candidates in all star-forming regions observed within the frame of the *Spitzer* c2d (Evans et al. 2009) and *Spitzer* Gould Belt[2] Legacy surveys (e.g., Spezzi et al. 2011; Peterson et al. 2011; Hatchell et al. 2012; Dunham et al. 2013).

In this section we provide a similar tool to identify class I/II YSO candidates on the basis of PACS/SPIRE colors. Such a tool is extremely useful for identifying probable YSOs when no complementary optical/near-IR observations are available, and can also be used to estimate the level of stellar contamination in *Herschel* extragalactic surveys. However, we stress that this is a very preliminary attempt because of the small amount of PACS/SPIRE fluxes for confirmed YSO and galaxy samples published so far.

We first collected from the literature PACS/SPIRE fluxes for confirmed YSOs. In addition to the 29 objects in Cha II, our final sample includes 49 objects in Cha I (Winston et al. 2012) and 28 objects in Serpens, for a total of 106 YSOs. Like Chamaeleon, Serpens is one of the clouds observed within the frame of the HGBS; the *Herschel* fluxes for the YSOs in this cloud were retrieved from the catalog obtained in Bressert et al. (2013), and a paper focused on this population is in preparation (Spezzi et al., in prep.). We also used, for comparison purposes, the PACS fluxes of ~50 young very low mass stars and brown dwarfs (BDs) published in Harvey et al. (2012b) and the predicted colors and flux densities of protostars in PACS and SPIRE filters in Ali et al. (2010); these colors are based on a grid of 20 160 model SEDs of low-mass protostars obtained by considering emission from four main components (a central object, a flared disk, a rotating collapsing envelope and a bipolar cavity) and varying their configuration parameters.

[2] http://www.cfa.harvard.edu/gouldbelt

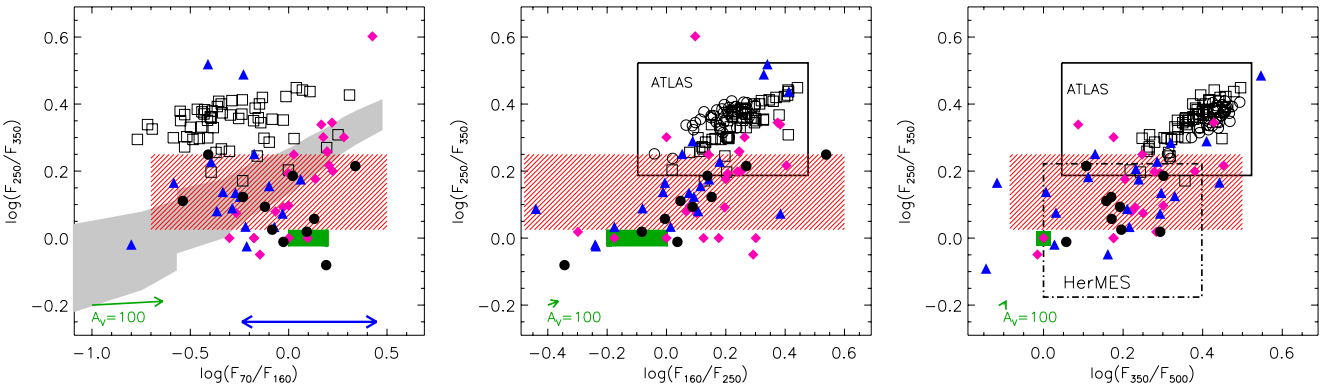

Fig. 4. PACS/SPIRE color–color diagrams, where colors are defined as the ratio logarithm of the flux densities in Jy measured in two different bands. The black filled circles are the YSOs in Cha II, while the magenta diamonds and blue triangles are YSOs in Cha I (Winston et al. 2012) and Serpens (Bressert et al. 2013), respectively. The red-striped areas mark the YSO loci proposed in this work. The open squares and circles represent the galaxy samples of Dale et al. (2012) and Corbelli et al. (2012), respectively. The green-filled area display the predicted colors for stellar photospheric emission. The arrow indicates the $A_V = 100$ mag reddening vector. The solid and dot-dashed lines in *the middle and right panels* indicate the loci of galaxies in the *Herschel*-ATLAS catalog and AGNs in the *Herschel*-HerMES survey, respectively. In the *left panel*, the gray-filled area is the protostar locus predicted in Ali et al. (2010), while the arrow-head line displays the $\log(F_{70}/F_{160})$ color range of the very low-mass stars and brown dwarfs in Harvey et al. (2012b).

We performed the same literature search for PACS/SPIRE fluxes of extragalactic sources and collected a sample of 96 galaxies: 35 galaxies in the Virgo cluster (Corbelli et al. 2012) and 61 nearby galaxies from the KINGFISH survey (Dale et al. 2012). The sample in the Virgo cluster consists of late-type star-forming galaxies, from weakly barred spirals (Sab) to irregular galaxies with no bulge component (Sm), some of them highly disturbed by the dense cluster environment. The KINGFISH sample includes galaxies spanning wide ranges in luminosity (over a factor of 10^4), optical/infrared ratio (over a factor of 10^3), metallicity, gas fraction, H_I/H_2 ratio, star formation rate, morphology, and bar strength; all normal galaxy types are represented and there are several galaxies with nuclei that are clearly distinguished by Seyfert or LINER characteristics, but none of them has an active galactic nucleus (AGN). We also used for comparison purposes i) the galaxy locus defined in Amblard et al. (2010) on the basis of sources detected by the *Herschel*-ATLAS (*Herschel* Astrophysical Terahertz Large Area Survey) observations, consisting of a flux-limited sample of about 2000 galaxies in the GAMA-9 field near the ecliptic plane, covering a wide range in redshift ($0 \lesssim z \lesssim 4$ with an average value of 2.2) and with an average dust temperature of ~28 K; ii) the active AGN locus defined in Hatziminaoglou et al. (2010) on the basis of the "*Herschel* Multi-tiered Extragalactic Survey" (HerMES) observations.

Finally, we estimated the expected colors of main-sequence stars and BDs without infrared excess emission at *Herschel* wavelengths, by convolving the stellar photosphere models of Hauschildt et al. (1999) and Allard et al. (2000) with the PACS/SPIRE filter response curves. We considered models with effective temperatures between 2000 and 10 000 K and $\log g = 5$, as appropriate for main sequence stars and BDs. We then investigated the variation of these synthetic colors as a function of reddening assuming the Weingartner & Draine (2001) extinction law for $R_V = 3.1$ (i.e., diffuse interstellar-medium).

We investigated the positions of these YSO, galaxy, and reddened photosphere samples on a combination of PACS/SPIRE CC diagrams, where colors are defined as the ratio logarithm of the flux densities measured in two different bands. Figure 4 illustrates three different PACS/SPIRE CC diagrams. Their inspection shows that the YSO population in Cha II, Cha I, and Serpens share the same color ranges and about 80% of the YSOs in these three clouds are confined in the following locus (indicated by the red-striped areas in the Fig. 4):

$$-0.7 \lesssim \log(F_{70}/F_{160}) \lesssim 0.5 \quad (1)$$

$$-0.5 \lesssim \log(F_{160}/F_{250}) \lesssim 0.6 \quad (2)$$

$$0.05 \lesssim \log(F_{250}/F_{350}) \lesssim 0.25 \quad (3)$$

$$-0.1 \lesssim \log(F_{350}/F_{500}) \lesssim 0.5. \quad (4)$$

These color ranges are consistent with the PACS/SPIRE colors predicted in Ali et al. (2010) for protostars and with the PACS colors of the sample of young very low-mass stars and BDs published in Harvey et al. (2012b). PACS/SPIRE colors of reddened photospheres are close to zero regardless of the assumed effective temperature and are unlikely to contaminate the YSO locus defined above, which is restricted to $\log(F_{250}/F_{350}) \gtrsim 0.05$, even assuming a very high extinction (i.e., $A_V = 100$ mag). Galaxies with a broad range of dust temperatures and redshifts (Amblard et al. 2010; Corbelli et al. 2012; Dale et al. 2012) occupy regions in PACS/SPIRE CC diagrams that marginally overlap with the YSO locus defined by us, with the expected level of contamination being about 10%. We performed a two-dimensional (2D) Kolmogorov-Smirnov (K-S) test in order to prove that the distribution of YSOs and galaxies in PACS/SPIRE CC diagrams are significantly different. We used the IDL routine *ks2d* developed by P. Yoachim[3]. This routine requires as input the two 2D arrays to be compared (which are in our case the SPIRE/PACS colors of the YSO and galaxy populations), and returns a probability close to 1, or at least not near zero, if the two populations were drawn from same parent distribution, and a probability close to 0 if this is not the case. Table 4 summarizes the results of the K-S test for the CC distribution in the three diagrams presented in Fig. 4. When comparing each of the YSO populations in Cha II, Cha I, and Serpens with the galaxy sample, we find a very low probability, about of 1.e-6 or even 1.e-9. Thus, the K-S test indicates that the distribution of the YSO populations on PACS/SPIRE CC diagrams is significantly different than the distribution of galaxies.

We therefore conclude that Eqs. (1)–(4) provide a reliable YSO selection tool when applied together, i.e., for YSOs meeting the four color conditions. Indeed, Fig. 4 (right panel) also

[3] http://www.as.utexas.edu/~yoachim/idl/py_idl.html

Table 4. Results of the 2D Kolmogorov-Smirnov test comparing the distribution of YSOs and galaxies in PACS/SPIRE CC diagrams (Fig. 4).

CC diagram	Probability[†] Cha II vs. galaxies	Probability[†] Cha I vs. galaxies	Probability[†] Serpens vs. galaxies
F_{250}/F_{350} vs. F_{70}/F_{160}	6.e-06	3.e-09	7.e-06
F_{250}/F_{350} vs. F_{160}/F_{250}	2.e-07	8.e-07	6.e-07
F_{250}/F_{350} vs. F_{350}/F_{500}	4.e-07	7.e-09	2.e-08

Notes. [(†)] The computed probability is 1 for two populations drawn from same parent distribution, and 0 for two populations with ideally different distributions.

indicates that when only SPIRE colors are available, YSOs cannot be singled out because of the high level of extragalactic contamination, in particular by AGNs, which share the same SPIRE colors as YSOs. However, as demonstrated in Hatziminaoglou et al. (2010), AGN samples can be very well separated from the non-AGN, star-forming galaxy populations, YSOs, etc., with a combination of *Spitzer*-MIPS and *Herschel*-SPIRE colors, specifically the $\log(F_{250}/F_{70})$ vs. $\log(F_{70}/F_{24})$ CC diagram. Indeed, as shown in Fig. 5, none of the YSOs in Cha II falls in the AGN area of this diagram.

4.1. Completeness of the YSO and galaxy samples

The lists of point-like sources observed with the HGBS published so far are limited to previously confirmed YSOs (this work; Winston et al. 2012; Ribas et al. 2013), because the nature of the other detected sources needs further confirmation. Thus, there is no systematic study of the photometric completeness of the survey. The same is true for some of the extragalactic surveys. Thus, we cannot systematically take into account completeness effects when defining the color ranges of YSOs and galaxies. However, we caution about the photometric completeness of the surveys used to collect our samples and, hence, the validity range of the YSO locus defined in Sect. 4.

As detailed in Sect. 4, the sample used to define the YSO locus was collected from HGBS observations of Cha II, Cha I, Serpens, and the catalog of young very low-mass stars and BDs by Harvey et al. (2012b). Although the source extraction was performed in each cloud using different tools, the HGBS observations were conducted in all clouds using the same observing strategy and, hence, photometric detection limits are quite similar. Our Cha II catalog has a 5σ detection limit of about 150 mJy at 70 and 100 μm and ~300 mJy at 160, 250, 350, and 500 μm (see Sect. 2 and Figs. 2–3). Winston et al. (2012) adopted the same strategy for source extraction in Cha I maps (i.e., *getsources*; Men'shchikov et al. 2012) and set a lower limit of 100 mJy in each PACS/SPIRE pass-band for reporting fluxes. Using CUTEX (Molinari et al. 2011), Bressert et al. (2013) found a point-like source detection limit for Serpens maps of about 300 mJy for PACS and 500 mJy for SPIRE. Finally, the catalog of Harvey et al. (2012b) contains an unbiased sample specifically selected to include young objects at or below the sub-stellar limit in nearby star-forming regions and all of them were detected above a 3σ level of a few mJy in PACS pass-bands. The overall YSO sample spans the spectral type range M/K, with only a handful of late G-type objects (e.g, see Table 2 of this paper, Table 1 in Winston et al. 2012; and Table 3 in Harvey et al. 2012b).

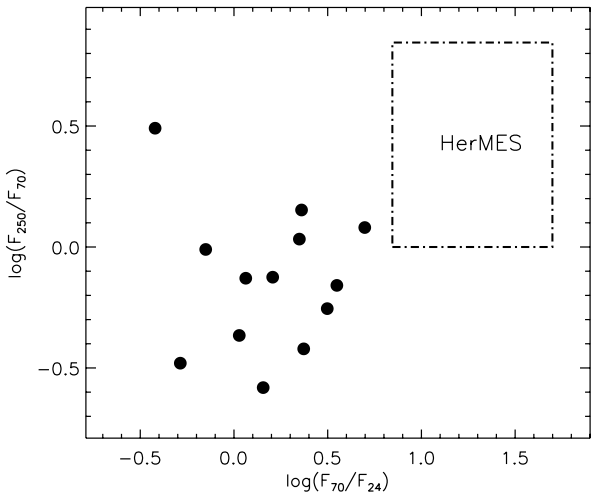

Fig. 5. log (F_{250}/F_{70}) vs. log (F_{70}/F_{24}) color–color diagram. The filled circles are YSOs in Cha II; their MIPS-24 μm fluxes were retrieved from the *Spitzer*-c2d catalog (Alcalá et al. 2008). The dot-dashed line indicates the locus of AGNs in the *Herschel*-HerMES survey (Hatziminaoglou et al. 2010).

The galaxy sample was collected from several extragalactic surveys conducted with *Herschel*. The sample in Corbelli et al. (2012) in the Virgo cluster is a magnitude-limited group of 35 type Sab to Sm galaxies, 100% complete down to 5 Jy with respect to the 250 μm flux. Dale et al. (2012) reported 1σ flux limits of 5, 2, 0.7, 0.4, and 0.2 MJy/sr at 70, 160, 250, 350, and 500 μm, respectively, for their sample of 61 nearby galaxies. The catalog assembled by Amblard et al. (2010) includes only galaxies detected in at least three of the PACS/SPIRE bands above the 5σ limit, which varies in the range 35–90 mJy depending on the pass-band. Finally, the SPIRE fluxes of AGNs reported in Hatziminaoglou et al. (2010) were collected considering all 5σ detections at 250 and 350 μm, corresponding to 12.8 mJy and 12.2 mJy, respectively, while no flux cut was applied at 500 μm.

We conclude that the YSO locus defined in Sect. 4 is valid for YSOs of spectral type M/K with fluxes above the HGBS 5σ limits, which are on the order of 100 mJy and 400 mJy for PACS and SPIRE pass-bands, respectively. The locus was defined by taking into account contamination from extragalactic sources with fluxes typically higher than 10–100 mJy in the specific pass-bands.

5. SED fitting and constraints on disk properties

One of the expected major outcomes from *Herschel* observations of class I/II YSOs is a better understanding of their circumstellar disks, in particular of the properties and geometry of their cool dust component where most of the mass is located (Harvey et al. 2012a). SED modeling is the most efficient way to derive these properties when the mid/far IR information comes exclusively from photometry, which is the case for the YSO sample in Cha II. However, as pointed out by several authors (e.g., Robitaille et al. 2007; Alcalá et al. 2008; Cieza et al. 2011), disk properties inferred from SED modeling are strongly model dependent and degenerate, meaning that more than one set of parameters is consistent with the observed SED. Therefore, they must be treated with extreme caution, used only for statistical purposes, and to provide typical ranges of disk parameter values.

Alcalá et al. (2008) and Spezzi et al. (2008) presented complete SEDs of the entire pre-main-sequence (PMS) populations

in Cha II from the optical to *Spitzer* wavelengths, together with reliable estimates of their stellar parameters (effective temperature, interstellar extinction, luminosity, radius, mass, age) based on follow-up optical spectroscopy. Based on the same dataset, Alcalá et al. (2008) also studied the structure of the circumstellar material around these objects using several sets of SED models for YSOs (Dullemond et al. 2001; D'Alessio et al. 2005; Robitaille et al. 2006). Because *Spitzer* IRAC and MIPS wavelengths preferentially probe the inner parts of the disk and only a few SEDs in their dataset were complete up to millimeter wavelengths, Alcalá et al. (2008) could provide constraints only on the inner disk structure and found a typical value for the disk inner radius on the order of 0.1 AU.

Merging the Alcalá et al. (2008) and Spezzi et al. (2008) datasets with the new HGBS observations, we have 26 YSOs in Cha II with complete SEDs from 0.4–0.5 μm up to 500–1300 μm, depending on available data, and robust stellar parameter estimates (Fig. 6). When available, we also included the fluxes at 3.4, 4.6, 12, and 22 μm from the Wide-field Infrared Survey Explorer (WISE; Wright et al. 2010) in the SED. Thus, in the following we attempt to constrain the properties of the cool dust in these 26 disks through SED modeling, with the aim of determining which disk parameters are the most likely to be constrained by our new HGBS data, and how. Note that, as said above, the HGBS retrieved 29 YSOs in Cha II. However, we do not attempt the SED fitting for IRAS 12522-7640, STc2d J130529.0-774140, and IRAS 13036-7644 because of the lack of optical/near-IR data for these objects[4].

To compare our modeling results with the previous modeling in Alcalá et al. (2008), we explored the same sets of models. However, as recently pointed out by Robitaille et al. (2012), the Robitaille et al. (2006) models are not sufficiently accurate at wavelengths beyond 100 μm and, hence, they are not appropriate to reproduce *Herschel* data; a new version of these models is currently in preparation (Robitaille 2011; Robitaille et al. 2012). The model grid by D'Alessio et al. (2005) is too coarse and does not allow us to take into account the exact stellar parameters of our YSO sample. Thus, we used the RADMC-2D code by Dullemond & Dominik (2004) (Version 3.1, July 2007) to compute SED models for the specific stellar parameters of our YSOs. RADMC-2D is an implementation of the 1D semi-analytic models (Dullemond et al. 2001) used in Alcalá et al. (2008).

5.1. Modeling setup

RADMC-2D is a two-dimensional Monte Carlo code for computing the radiative transfer through an axisymmetric configuration of dust (Dullemond & Dominik 2004)[5]. The disk is assumed to be passive, i.e., non-accreting, so that the energy balance is entirely determined by the irradiation from the central star[6]. Several of the YSOs in Cha II have a significant mass accretion rate (Spezzi et al. 2008; Alcalá et al. 2008); however, the presence of mass accretion is expected to affect the SED shape mainly at UV/optical wavelengths, producing an excess emission due to the hot gas in the internal accreting envelope, hot spots on the stellar surface heated by the accreting columns, etc. (Feigelson & Montmerle 1999), while we use our modeling results only to explore the outer regions of the disk probed by *Spitzer/Herschel* wavelengths (Sect. 5.2).

The main input parameters of RADMC-2D are the density structure of the dusty circumstellar material, the dust opacity tables, and the stellar parameters. The output is the dust temperature structure, the scattering source functions, and a set of SEDs at various inclination angles. For each YSO in our sample, we computed a grid of SED models. Because we do not have mid/far IR spectra of our sources and millimeter fluxes are available only for a few of them, we cannot put constraints on the mineralogy and the grain size distribution of the dust and expect to probe dust properties within a few hundred AU from the central star. On the other hand, we have detailed information of the stellar properties, which allows us to eliminate some of the degeneracy in the model SEDs. Thus, the following parameters were fixed in all models:

1. For each object, we fixed the stellar mass ($M_\star$), radius ($R_\star$), and effective temperature ($T_{\rm eff}$) to the values spectroscopically determined in Spezzi et al. (2008) and reported in Table 5. RADMC-2D adopts the Kurucz stellar atmosphere models[7] for the stellar input if the object's $T_{\rm eff}$ is $\geq$3500 K, while for colder objects a blackbody emission is assumed. We note that for four of our objects (namely IRAS 12416-7703, ISO-CHAII 28, IRASF 12571-7657, and IRAS 12589-7646) the stellar mass could not be estimated from optical data (see Sects. 4.5 and 4.7 in Spezzi et al. 2008), although their spectral type indicates that they are not substellar objects. Thus, for these three objects we estimated the stellar mass, together with the disk parameters, from the best-fitting SED model, considering only models with the same $T_{\rm eff}$ as the object. For IRAS 12500-7658 Spezzi et al. (2008) reported a $T_{\rm eff}$ of 2900 K (see their Sect. 4.7); however, follow-up spectroscopy with VLT/FORS2 revealed an earlier spectral type close to K5, although the object is strongly veiled (Alcalá, priv. comm.), and this is the value we adopted for our modeling.
2. We fixed the slope of the grain size distribution: $\mathrm{d}n(a) \propto a^{-3}\mathrm{d}a$, with minimum grain size $a_{\rm min} = 0.1$ μm and maximum grain size $a_{\rm max} = 1$ cm. This range is consistent with the values inferred from the analysis of SED slopes at millimeter wavelengths of T Tauri disks (Rodmann et al. 2006; Lommen et al. 2007; Ricci et al. 2010; Ubach et al. 2012).
3. We assumed the typical chemical composition of dust grains in protoplanetary disks as in Ricci et al. (2010), i.e., porous composite spherical grains made of astronomical silicates (optical constants from Weingartner & Draine 2001), carbonaceous materials (Zubko et al. 1996), and water ices (Warren 1984), with fractional abundances from a simplification of the model used in Pollack et al. (1994) and a volume fraction for vacuum of ~30%.
4. We assumed a gas-to-dust mass ratio of 100 (Dutrey et al. 2004, and references therein).
5. We fixed the outer disk radius at 200 AU. As shown in Harvey et al. (2012a) and Cieza et al. (2011), the choice of the outer radius makes essentially no difference to the model SED in the spectral range of our study (typically

[4] IRAS 12522-7640 and IRAS 13036-764 were fist detected by IRAS at mid-to-far IR wavelengths; IRAS 12522-7640 is unclassified, while and IRAS 13036-7644 has been reported by Lehtinen et al. (2005) to be a transition object between Class 0 and I. STc2d J130529.0-774140 was first detected at mid-IR wavelengths by the *Spitzer*-c2d survey (Alcalá et al. 2008) .

[5] http://www.mpia-hd.mpg.de/~dullemon/radtrans/radmc/

[6] To what extent active accretion changes the stellar flux impinging on the disk surface and, hence, the thermal equilibrium in the disk is yet to be determined (e.g., Wood et al. 2008); however, this discussion is beyond the scope of this paper.

[7] http://www.stsci.edu/hst/observatory/cdbs/k93models.html

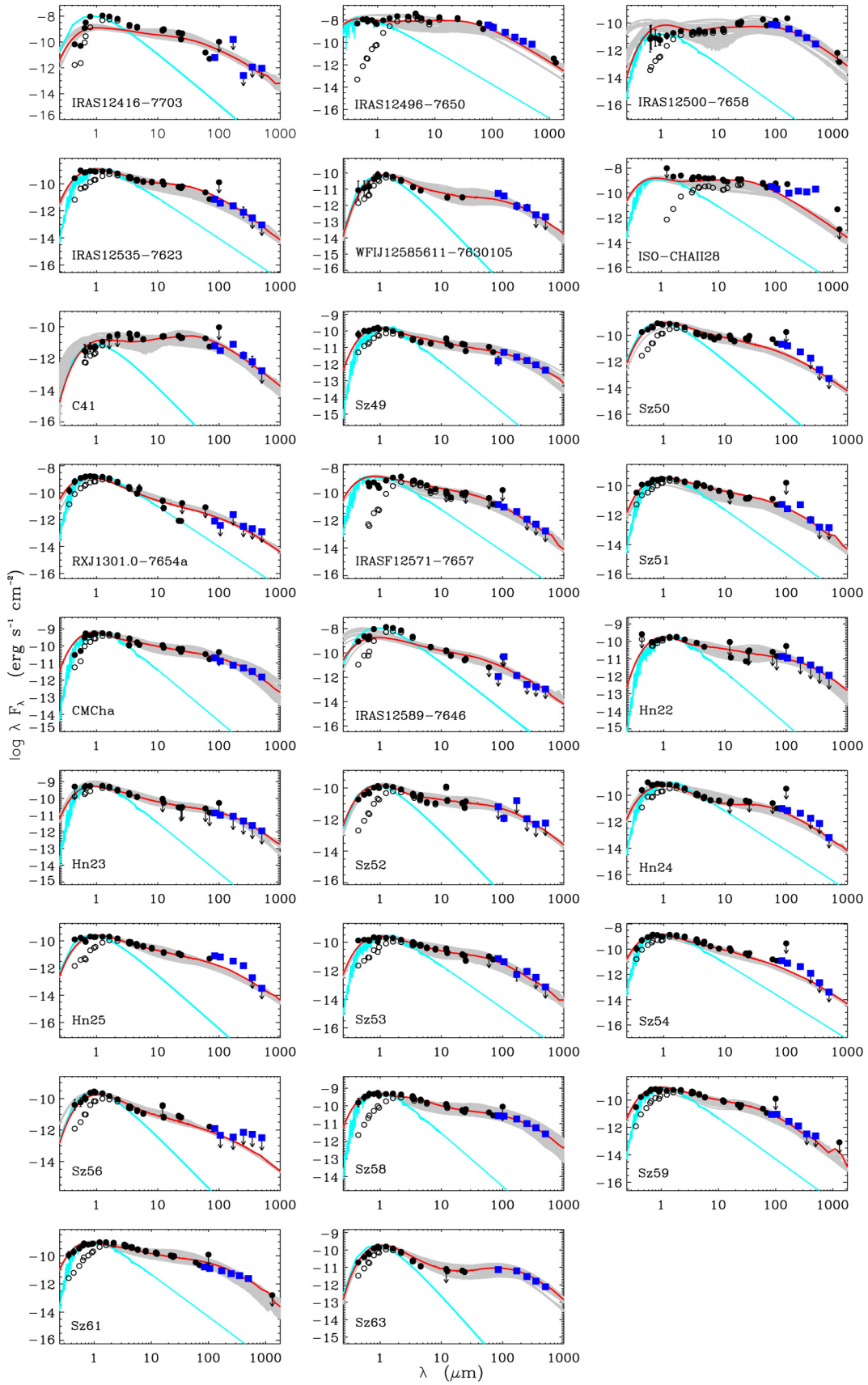

Fig. 6. Observed (open circles) and dereddened (dots) spectral energy distributions of known YSOs in Cha II detected with the HGBS. The squares mark PACS and SPIRE fluxes, while the dots are optical-to-infrared flux measurements from previous surveys (Alcalá et al. 2008). The Kurucz's model spectrum (for objects with $T_{\rm eff} \geq 3500$ K) or the blackbody spectrum (for objects with $T_{\rm eff} < 3500$ K) with the same $T_{\rm eff}$ as the object and scaled to its distance and radius (Spezzi et al. 2008), is overplotted on each SED, representing the stellar flux. The red thick line is the best-fitting RADMC-2D SED model, while the gray lines display the first 100 best-fitting SED models.

Table 5. Stellar properties and most probable disk parameters for the known YSOs in Cha II detected by the HGBS.

Main designation	$T_{\rm eff}$[†] [K]	A_V[†] [mag]	$R\star$[†] [$R_\odot$]	$M\star$[†] [$M_\odot$]	$R_{\rm in}$[♣] [AU]	$R_{\rm C}$[♣] [AU]	$M_{\rm disk}$[♣] [$M_\odot$]	Flaring angle[♣] [$1+\phi$]	Inclination angle[♣] [deg]	ε_0
IRAS 12416-7703	3487	3.36	3[♠]	2[♠]	0.02–0.1 (32%)	>5 (27%)	>0.001 (40%)	1.1 (26%)	40 (33%)	1.17
IRAS 12496-7650	7200	10.55	2.77	2	0.05–0.1 (33%)	>50 (20%)	>0.1 (50%)	1.3–1.4 (25%)	10 (35%)	0.39
IRAS 12500-7658[⋆]	4350	6.85	1.00	0.60	0.1 (33%)	>10 (19%)	>0.01 (36%)	1.3–1.4 (26%)	40 (27%)	0.61
IRAS 12535-7623	3850	3.36	2.71	0.67	0.02 (34%)	>50 (23%)	>0.0001 (99%)	1.1–1.4 (25%)	70 (28%)	0.18
WFI J12585611-7630105	3025	1.66	1.13	0.12	0.02–0.1 (33%)	>150 (20%)	>0.0001 (59%)	1.3 (25%)	70 (26%)	0.07
ISO-CHAII 28	4500	38.9	2.5[♠]	1.5[♠]	0.02 (34%)	>10 (37%)	>0.01 (36%)	1.1 (27%)	10 (34%)	1.32
C 41	3057	2.17	0.37	0.10	0.05–0.1 (30%)	>5 (25%)	>0.0001 (50%)	1.1 (30%)	90 (36%)	0.28
Sz 49	3777	2.28	1.03	0.62	0.05–0.1 (34%)	>100–200 (17%)	>0.001 (28%)	1.3–1.4 (25%)	10–70 (29%)	0.07
Sz 50	3415	3.78	3.10	0.35	0.02–0.05 (33%)	>100 (27%)	>0.0001 (99%)	1.1–1.4 (25%)	90 (27%)	0.61
RX J1301.0-7654a	4350	1.93	2.67	0.7	0.02 (29%)	>100 (24%)	>0.0001 (86%)	1.1 (26%)	40 (35%)	0.40
IRASF 12571-7657	4730	9.03	2[♠]	1[♠]	0.02 (34%)	>10 (18%)	>0.0001 (92%)	1.1 (30%)	70 (28%)	0.44
Sz 51	3955	1.54	1.37	0.7	0.02–0.1 (33%)	>50 (25%)	>0.0001 (99%)	1.1 (26%)	10–90 (25%)	0.35
CM Cha	4060	1.52	1.78	0.85	0.1 (34%)	>10–50 (17%)	>0.01 (28%)	1.4 (26%)	10–70 (29%)	0.18
IRAS 12589-7646	3300	3.98	2.8[♠]	2[♠]	0.02 (31%)	>100 (21%)	>0.0001 (88%)	1.1 (27%)	40 (33%)	0.67
Hn 22	3560	0.61	1.24	0.42	0.05–0.1 (34%)	> 5 (23%)	>0.001 (36%)	1.2 (26%)	70 (30%)	0.23
Hn 23	4350	1.24	1.60	1	0.02–0.1 (31%)	> 5 (19%)	>0.001 (45%)	1.1 (26%)	40 (31%)	0.07
Sz 52	3487	4.14	1.15	0.35	0.02–0.1 (31%)	>100 (21%)	>0.0001 (54%)	1.2? (25%)	40 (30%)	0.25
Hn 24	3850	2.76	2.37	0.65	0.02–0.1 (33%)	>50 (26%)	>0.0001 (99%)	1.4 (26%)	90 (26%)	0.52
Hn 25	3487	4.10	1.56	0.3	0.02 (34%)	>150 (26%)	>0.0001 (100%)	1.2 (28%)	10–90 (25%)	0.26
Sz 53	3705	3.68	1.39	0.55	0.02-0.1 (33%)	>50 (19%)	>0.0001 (97%)	1.1 (27%)	70 (28%)	0.10
Sz 54	4350	1.57	2.42	0.97	0.02 (33%)	>150 (39%)	>0.0001 (99%)	1.1–1.2 (30%)	10–70 (25%)	0.63
Sz 56	3270	3.18	1.78	0.23	0.02 (39%)	>200 (44%)	>0.0001 (89%)	1.1 (30%)	90 (28%)	0.37
Sz 58	4350	3.87	1.43	1	0.1 (33%)	>10 (17%)	>0.01 (29%)	1.3–1.4 (25%)	10–40 (31%)	0.04
Sz 59	4060	2.67	1.96	0.82	0.02–0.05 (34%)	>10–200 (18%)	>0.0001 (91%)	1.1 (29%)	10–70 (27%)	0.28
Sz 61	4350	3.13	1.87	1	0.02–0.1 (33%)	>10 (21%)	>0.01 (34%)	1.3 (26%)	10–70 (30%)	0.15
Sz 63	3415	1.61	1.38	0.32	0.05–0.1 (33%)	>200 (17%)	>0.001 (27%)	1.4 (27%)	10–70 (28%)	0.04

Notes. For the disk parameters, we indicate the relative Bayesian probability in percentage between brackets. When several values of a given disk parameter are equally probable (i.e., partly flat Bayesian probability distribution, Figs. 7, 8), we report the compatible range. Disk mass ($M_{\rm disk}$) and size ($R_{\rm C}$) should be regarded as lower limits (Sect. 5.1). In the last column, we report the value of the intrinsic scatter (ε_0) between the observed SED and the best-fitting SED model. [(†)] From Spezzi et al. (2008). [(♠)] The values sample by the grid are as follows: $R_{\rm in}$ = [0.02, 0.05, 0.1, 0.5, 1, 5, 10] AU, $R_{\rm C}$ = [5, 10, 50, 100, 150, 200] AU, $M_{\rm disk}$ = [0.0001, 0.001,0.01, 0.1] $M_\odot$, $1+\phi$ = [1.1, 1.2 ,1.3 ,1.4] and Inclination=[10, 40, 70, 90] deg. [(♠)] Stellar mass and radius not provided in Spezzi et al. (2008). The values reported here are estimated from the best-fitting SED model, considering only models with the same $T_{\rm eff}$ as the object. [(⋆)] Stellar parameters are estimated assuming spectral type K5 (Alcalá; priv. comm.).

0.4–500 μm). This is because for sub-solar mass objects, as those in our sample (Table 5), most of the IR emission probed by *Spitzer*/*Herschel* data comes from dust at radii inside of ∼200 AU.

6. The surface density profile was set to

$$\Sigma(R) = \Sigma_0 \cdot \exp\left[-\left(\frac{R}{R_{\rm C}}\right)^{\rm plsig}\right],$$

where $R_{\rm C}$ is the characteristic radius beyond which the surface density distribution rapidly declines to zero. The power law exponent (plsig) was set to –1 at radii smaller than $R_{\rm C}$ and to –12 at radii larger $R_{\rm C}$. Σ_0 is the surface density at $R_{\rm C}$ and depends on $R_{\rm C}$ and the disk mass ($M_{\rm disk}$): $\Sigma_0 = \frac{M_{\rm disk}}{2\pi R_{\rm C}^2}$.

Note that these assumptions are consistent with our current understanding of disks around T Tauri stars (e.g., Williams & Cieza 2011) and with the assumptions made by other authors who explored SED modeling that included *Herschel* photometric data (Cieza et al. 2011; Harvey et al. 2012a,b). This makes our results easily comparable with other YSO disk-modeling results.

On the other hand, the spectral range covered by our SEDs is expected to probe the inner disk properties through the near/mid IR emission, and *Herschel* observations at longer wavelengths are expected to be more sensitive to the disk mass and degree of flaring (e.g., Harvey et al. 2012a,b). Thus, for each YSO in our sample, a grid of 2700 SED models was created by varying the following parameters in specific ranges:

1. We explored seven different values for inner disk radius ($R_{\rm in}$): 0.02, 0.05, 0.1, 0.5, 1, 5, and 10 AU. This choice covers the typical range of dust sublimation radii expected for T Tauri stars in our effective temperature range (Williams & Cieza 2011) and also includes some higher values expected for transition objects with inner holes (e.g., Muzerolle et al. 2010; Merín et al. 2010).
2. We left the pivot point of the density distributions ($R_{\rm C}$) to vary between 5 and 200 AU. $R_{\rm C}$ is the characteristic radius beyond which the density distribution rapidly declines to zero. Obviously, it must be similar to or smaller than the actual disk outer radius (fixed at 200 AU in our case) and provides an estimate of the size of the disk region probed by our near-IR to sub-mm photometry, i.e., a lower limit to the actual disk size.
3. We explored four different values for the disk mass (gas and dust, $M_{\rm disk}$): 0.0001, 0.001, 0.01, and 0.1 $M_\odot$. These values cover the typical range expected for class II YSOs (see Fig. 1 by Williams & Cieza 2011). Disk masses are well measured at sub-mm/mm wavelengths, where disks are optically thin (i.e., vertical optical depth $\tau < 1$) and the dust is virtually all-emitting in this range (i.e., Harvey et al. 2012b). However, for most of our objects, flux measurement are available up to 500 μm and disks with the typical geometry and range of parameters ($R_{\rm in}$, $M_{\rm disk}$, $a_{\rm max}$) explored by us, not observed edge-on, may still emit a few percent of the total flux at optical depth $\tau > 1$ at this wavelength. Thus, the $M_{\rm disk}$ derived from our SED modeling must be regarded as a lower limit for the actual disk mass.
4. Protoplanetary disks are flared with a vertical scale height (H) that increases with radius. We assumed a

parametrized power law dependency: $H(R) = H_{R_C} \cdot [\frac{R}{R_C}]^{1+\phi}$. H_{R_C} is the vertical pressure scale height at R_C, and we set it to 0.15 in unit of radius, a fiducial hydrostatic equilibrium value. We left the flaring angle (ϕ) to vary between 0.1 and 0.4 in step of 0.1 (i.e., $1.1 \leq 1 + \phi \leq 1.4$), consisten with the analytical/numerical values found in previous studies (Chiang & Goldreich 1997; D'Alessio et al. 1998; Dullemond et al. 2002).

5. We computed each model SED at four inclination angles with respect to the line of sight: 10, 40, 70, and 90 degrees, i.e., between the face-on (0 deg) and edge-on (90 deg) configuration. The inclination angle is poorly determined from SED modeling alone, a well-known result from previous works (D'Alessio et al. 1999; Chiang & Goldreich 1999; Robitaille et al. 2007; Alcalá et al. 2008). However, one needs to state the ranges of inclinations that provide a good fit, as there is in some cases a degeneracy between disk size/mass and inclination (Robitaille et al. 2007).

With this configurations of free parameters, we reached a compromise between a sufficiently accurate SED model grid for each YSO and a reasonable computational time.

5.2. Modeling results

We used an ad hoc fitting routine developed under IDL[8] to select which of the 2700 model SEDs best fits the observed SED for each YSO. Prior to the fit, the model grid was scaled to the Cha II distance (178 pc) and each observed SED was dereddened using the A_V values derived in Spezzi et al. (2008) and reported in Table 5.

For several of our YSOs only flux upper limits are available at certain wavelengths (see Table 2) and, hence, our SED fitting has to deal with partly censored data. We adopted the likelihood-based approach of Kelly (2007), implemented by these authors in the IDL routine *linmix_err.pro*[9], to determine the best-fitting SED model taking simultaneously into account observed flux errors and upper limits. This routine assumes a linear correlation between the dependent and independent variable (i.e., model and observed fluxes, in our case) and performs a Bayesian linear regression to determine the slope, the normalization, and the intrinsic scatter of the relationship. The probability model approximates the distribution of the independent variable as a mixture of Gaussians functions. Since a direct computation of the posterior distribution is too computationally intensive, random draws from the posterior distribution were obtained using a Markov chain Monte Carlo method (see Sect. 6.2 by Kelly 2007). The derived likelihood function is modified by including an indicator variable (D), which is equal to 1 for true detections and equal to zero for censored data (i.e., flux upper limits in our case). The censored data were taken into account by marginalizing over them when computing the posterior, using the Metropolis-Hastings algorithm (Metropolis et al. 1953). The intrinsic scatter of the regression (ε_0) was assumed to be normally distributed and, analogously to the χ^2, provides an estimate of the goodness of fit of the observed distribution to the theoretical one; the lower ε_0, the better the quality of the fit and, hence, the best-fitting SED model is determined by minimizing ε_0.

Since SED modeling is known to be highly degenerate, the best-fit model is unlikely to be a unique solution and should be treated with caution. We therefore adopted the Bayesian method (e.g., Pinte et al. 2008) to calculate the probability of the disk parameter values sampled by the grid given the available data. For each disk parameter, if we assumed no prior knowledge on its value, the relative probability of a given model is proportional to $e^{-\varepsilon_0/2}$. All probabilities were normalized so that the sum of all the probabilities of the models in the grid is equal to 1. Figures 7 and 8 show the probability distribution of each disk parameter for each YSO in the range of values sampled by our grid. A very flat probability distribution indicates that the given parameter its not well constrained (i.e., many/all values sampled by the grid are equally possible). Clearly, some parameters are better constrained than others, for some objects more than for others, depending on the available SED data. In Table 5 we report the most probable disk parameters (R_{in}, R_C, M_{disk}, flaring angle, and inclination angle) and the computed ε_0 for the best-fitting model; when several values of a given disk parameter are equally probable (i.e., partly flat Bayesian probability distribution), we report the compatible range.

In Fig. 6 we show the SEDs of the 26 YSOs detected in Cha II with the HGBS together with the best-fitting RADMC-2D SED model and the first 100 best-fitting SED models (i.e., higher probability models). Note that the SED fitting for IRAS 12416-7703, IRAS 12500-7658, and IRAS 12589-7646 is not optimal at optical/near-IR wavelengths ($\lesssim$1 μm). IRAS 12500-7658 is a class I source, and IRAS 12416-7703 and IRAS 12589-7646 have not been observed through spectroscopy and, hence, their spectral types are inferred from broad-band photometry alone (Spezzi et al. 2008; Alcalá et al. 2008). Thus, the difficulty in modeling the stellar contribution to the SED of these objects probably derives from an inaccurate estimate of their stellar parameters (visual extinction and T_{eff}), stellar variability, and/or the presence of an active accreting disk, which affects the total energy balance; indeed, this last effect is not taken into account by RADMC-2D, which assumes a passive disk and irradiation from the central star only. However, the SED beyond 1 μm and up to the far-IR is well reproduced by the models and, hence, the extracted disk parameters are as reliable as for the other objects (see also discussion in Sect. 5.1). For a few objects (ISO-CHAII 28, Sz 50, Hn 25, and Sz 54) the best-fitting SED model appears to underestimate the far-infrared flux ($\lambda \gtrsim 100\,\mu$m); these objects are located in the region of Cha II with strongest background emission and, hence, the measured flux densities might be contaminated. We also note that the SEDs of the Class I object IRAS 12500-7658 is well reproduced at IR wavelength ($\gtrsim$1 μm) by the disk emission alone, without considering the presence of an envelope, which is normally invoked to model the SEDs of Class I YSOs (e.g., Lommen et al. 2008).

5.3. Discussion

Estimating some disk parameters (R_{in}, R_C and M_{disk}) through SED modeling was already attempted for the Cha II sample in Alcalá et al. (2008) on the basis of optical and *Spitzer* imaging (see their Tables 8 and 9). While R_{in} is expected to be fairly well constrained with *Spitzer* data, the R_C and M_{disk} values derived by us are expected to be more accurate than previous estimates, because we used an extended SED dataset that includes *Herschel* fluxes up to 500 μm. Moreover, thanks to the new HGBS data, we also tried to estimate the degree of flaring ($1 + \phi$) of these disks, which was never attempted before.

In this section, we discuss the disk parameters derived in Sect. 5.2 in more detail, comparing them with previous results

[8] Interactive Data Language.

[9] http://idlastro.gsfc.nasa.gov/ftp/pro/math/linmix_err.pro

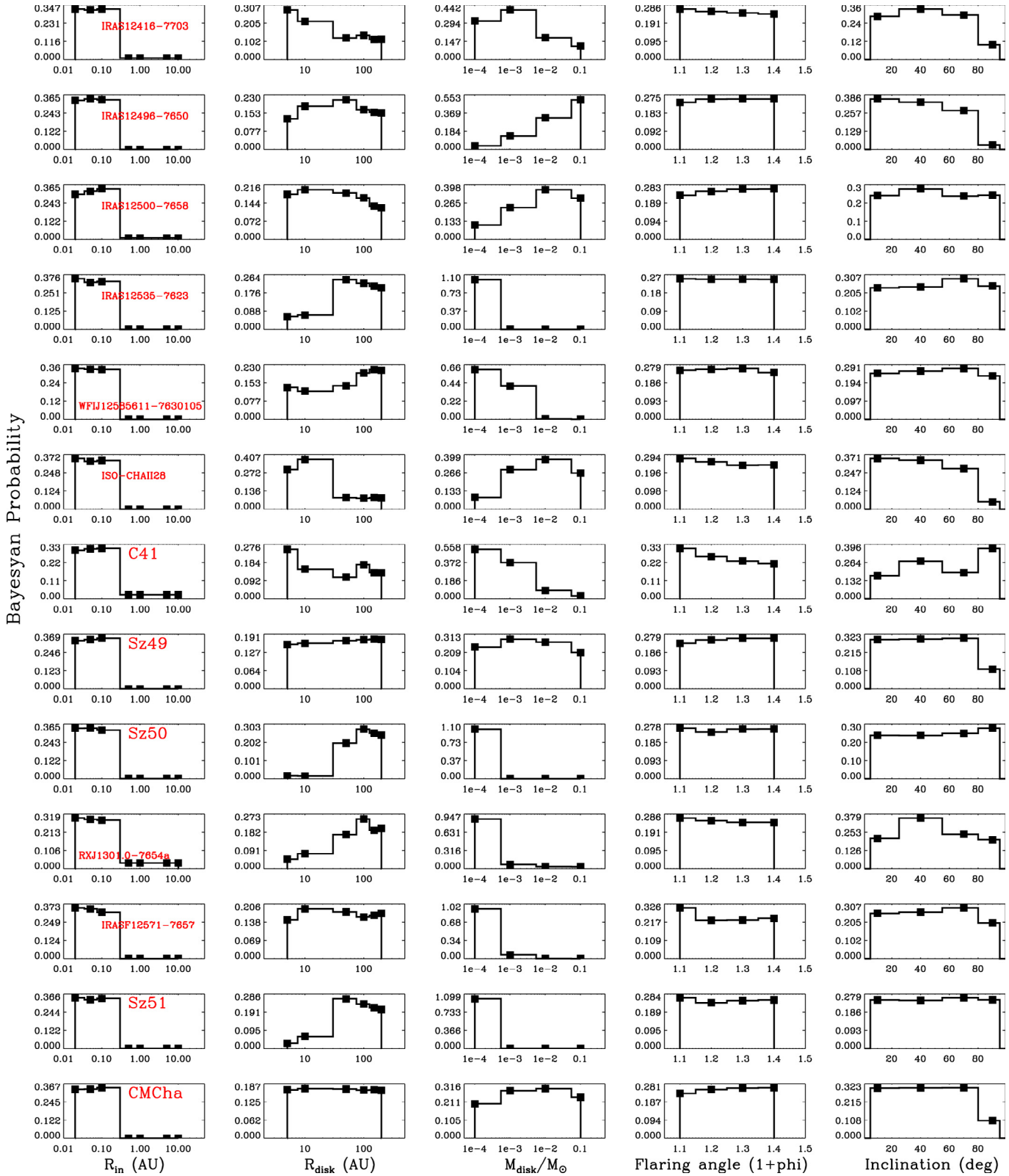

Fig. 7. Bayesian probability distribution of the five free-disk parameters in our SED modeling for the entire SED model grid computed for each YSO.

of Alcalá et al. (2008) and cautioning on their use. We start with a general and very important caution that applies to the use of all disk parameter values reported in Table 5: because of the large uncertainty/degeneracy of SED modeling results (outlined in Sect. 5), *these values must be used as indications of the order of magnitude of each disk parameter for the Cha II sample and for statistical purposes only, while values for individual objects are likely to have large uncertainties*.

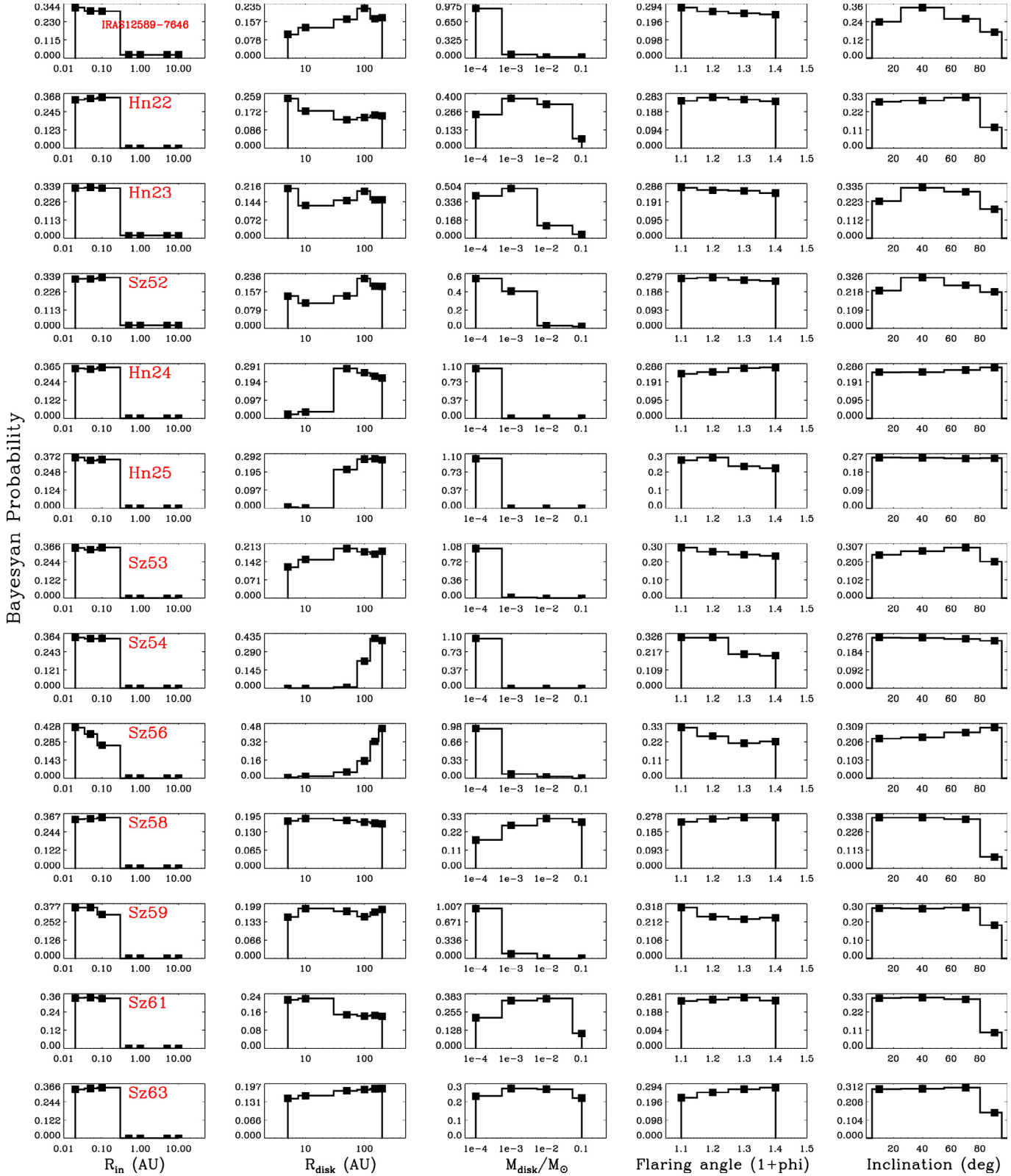

Fig. 8. Same as Fig. 7.

$R_{\rm in}$: our SED model grid explores seven values for the inner disk radius covering the range of dust-sublimation radii expected for T Tauri stars in our $T_{\rm eff}$ range and including larger radii expected for transition objects (Sect. 5.1). The choice of this loose grid in $R_{\rm in}$ was motivated by the fact that as accurate $R_{\rm in}$ values as are possible have been presented in Alcalá et al. (2008) for the Cha II YSO sample using *Spitzer* data and several SED models (Robitaille et al. 2006; Dullemond et al. 2001; D'Alessio et al. 2005). Thus, we aimed at roughly estimating the range of $R_{\rm in}$ values for this sample and confirming the results of Alcalá et al. (2008) on the basis of an SED dataset that is now more complete in the near/mid IR, because it includes WISE and PACS data.

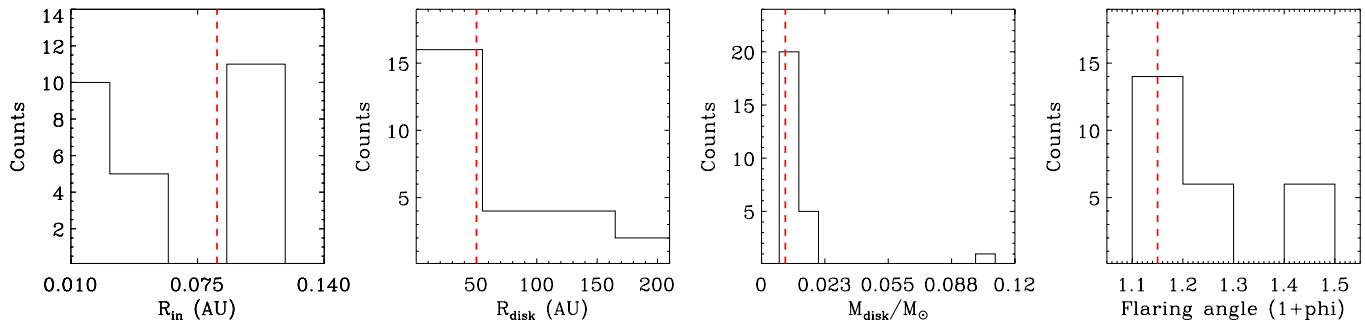

Fig. 9. Distribution of four free-disk parameters in our SED modeling for 26 YSOs in Cha II detected with the HGBS. We do not show the distribution of the disk inclination angles, because it is poorly constrained by the SED modeling (Sect. 5.3). The dashed lines indicates the median value of each distribution.

Considering the many uncertainties in SED modeling, our values agree fairly well with the the estimates in Alcalá et al. (2008), the relative difference is on the order of 30%. We also confirm a typical value for the disk inner radius for the Cha II sample of about 0.1 AU or lower (Fig. 9), with a dispersion of 0.04 AU; considering the stellar radii reported in Table 5, this value corresponds to typical inner radii ∼7 times larger than the stellar radius. We note that, although our grid does not extend beyond 10 AU, none of the 26 objects investigated here has the characteristic SED of transition objects with larger inner holes; the Bayesian probability distributions (Figs. 7, 8) indicate that inner radii larger than 0.1 AU appear to be inconsistent with the SEDs of all our objects. For most of them, the $R_{\rm in}$ Bayesian probability distribution presents a clear peak, indicating that this parameter is fairly well constrained for our sample, as expected because of the good SED coverage at near-to-mid IR wavelengths. Assuming our $R_{\rm in}$ values and using Eq. (11) of Dullemond et al. (2001), we also estimated the blackbody temperature of the disk inner rim ($T_{\rm rim}$) for our sample; depending on the spectral type of the object, $T_{\rm rim}$ spans the range 1000–2500 K, with a typical value around 1500 K, consistent with the dust sublimation temperature (typically 900-1600 K for silicates; e.g., Duschl et al. 1996).

$R_{\rm C}$: as clarified in Sect. 5.1, $R_{\rm C}$ is the characteristic radius beyond which the disk density distribution rapidly declines to zero; it provides an estimate of the size of the disk region probed by our photometry ($\lesssim$500 μm) and should be regarded as a lower limit to the actual disk size. The typical value of $R_{\rm C}$ for the Cha II sample is ∼50 AU and the dispersion is as high as 60 AU (Fig. 9). On average, our values are higher than the estimates provided in Alcalá et al. (2008) and the typical difference is on the order of 50%. This systematic difference probably arises from the better sampling of our SEDs beyond 70 μm. The $R_{\rm C}$ Bayesian probability distributions present a clear peak for the majority of the objects (Figs. 7–8), supporting the reliability of our estimates. We recall that we assumed a power law exponent plsig = −1 for the surface density profile at radii smaller than $R_{\rm C}$ (Sect. 5.1); a steeper profile (i.e., higher values of plsig) would produce larger $R_{\rm C}$ (see discussion in Ricci et al. 2013).

$M_{\rm disk}$: as for the disk size, the lack of data at mm-wavelengths for the majority of our objects prevents us from giving a reliable estimate of the total disk mass, and the values provided in Table 5 should be regarded as lower limits. On the other hand, *Herschel* observations at 500 μm are expected to be sensitive to the disk mass (e.g., Harvey et al. 2012a,b) and, indeed, we find a large difference (∼80%) between our values and the previous estimates in Alcalá et al. (2008); we note, however, that part of this difference is due to different assumptions on the chemical composition of dust grains and, hence, on the dust opacity. Our $M_{\rm disk}$ Bayesian probability distributions present a clear peak for most of the objects (Figs. 7–8), supporting the reliability of our estimates. The typical value for the Cha II sample is ∼0.0001 $M_{\odot}$ and the dispersion around this value is 0.9 dex (Fig. 9). Thus, the disk mass distribution in Cha II appears to be similar to that observed in Andrews & Williams (2005) in the Taurus-Auriga star formation region (typical disk mass 5×10^{-3} $M_{\odot}$ and dispersion 0.5 dex) on the basis of a sub-mm survey (350−850 μm) of about 150 YSOs in the same stellar mass range, and higher than the median values (3×10^{-5} $M_{\odot}$) estimated in Harvey et al. (2012b) for a sample of ∼50 lower-mass stars and BDs on the basis of PACS-only data. Considering the typical mass of our YSOs (Table 5), we find that the lower limits to the disk mass are proportional to the stellar masses with a 0.3% ratio, again very similar to the typical value in Taurus-Auriga (0.5%; Andrews & Williams 2005) and in the range ($\lesssim$1%) estimated for young Class II stars and BDs across a broad range of stellar masses (0.015–3 $M_{\odot}$; Klein et al. 2003; Andrews & Williams 2005; Scholz et al. 2006). This approximately constant disk-to-stellar mass ratio, together with recent observational studies that revealed stellar-mass dependence for other disk properties, such as mass accretion rate (e.g., Natta et al. 2004; Muzerolle et al. 2005), disk lifetime (e.g., Carpenter et al. 2006; Pascucci & Tachibana 2010) and disk organic chemistry (e.g., Pascucci et al. 2009), indicates that disk properties depend on stellar properties, in contrast with the assumptions of some models of planet formation (see discussion in Szűcs et al. 2010; Kornet et al. 2006).

Flaring index ($1 + \phi$): *Herschel* observations at far-IR wavelengths (250–500 μm) are expected to be sensitive to the degree of flaring (e.g., Harvey et al. 2012a,b), and the estimate of this parameter has not been attempted before for the Cha II sample. However, Figs. 7-8 show that the $1 + \phi$ Bayesian probability distributions has a tentative trend for some of our YSOs, while is partly flat for others. Thus, the flaring angle is poorly constrained for our sample; this uncertainty arises from the fact that for several of our YSOs only flux upper limits are available in the wavelengths range 250–500 μm. Keeping this limitation in mind, we observe a preferential value around 1.1–1.2, i.e., a low degree of flaring for the great majority of the objects (Fig. 9). To understand the meaning of these preferentially low values for the flaring angle, we recall that $1 + \phi$ describes the changing of the pressure scale height (H) with the radius (Sect. 5.1); a flatter disk has a lower H than a flared disk at the same emitting region. Thus, lower $1 + \phi$ values, as typical for our sample, indicate that H increases more slowly with the radius and, hence, the disk is flatter. Considering that our objects have spectral types of late K

to late M, this result is consistent with the finding of Szűcs et al. (2010) in the nearby Chamaeleon I association based on a sample of 200 G to late M-type stars. Although their study is based on *Spitzer* IRAC/MIPS data only and, hence, their flaring estimates are even less robust than ours, these authors found indications that disks around lower-mass stars in Chamaeleon I are statistically flatter than those of coeval higher mass stars in the same region. Harvey et al. (2012b) also estimated for their ~50 very low-mass stars and BDs detected with *Spitzer* and *Herschel*/PACS a typically low flaring angle (1.1–1.2, see their Fig. 14). This apparent flaring/spectral type anti-correlation has been suggested for several years on the basis of observational studies (Apai et al. 2002; Pascucci et al. 2003; Apai et al. 2005; Szűcs et al. 2010), although disk models predict the opposite (Walker et al. 2004), and it additionally supports the idea that disk properties show a dependence on stellar properties.

Inclination angle: the disk inclination angle is poorly determined from SED modeling alone (D'Alessio et al. 1999; Chiang & Goldreich 1999; Robitaille et al. 2007; Alcalá et al. 2008), a result confirmed by the very flat Bayesian probability distribution observed for the great majority of our YSOs (Figs. 7–8). Thus, the values reported in Table 5 must be regarded as ranges of inclination that provide a good SED fit. As previously mentioned, it is important to state this range, because in some cases there is a degeneracy between disk size/mass and disk inclination (Robitaille et al. 2007).

5.3.1. Note on Hn 24

Hn 24 is a class II YSO of spectral type M0 and stellar mass ~0.65 $M_{\odot}$ (Table 5). The circumstellar material around this object has been extensively studied in Merín et al. (2010). The object was proposed to be a cold-disk candidate (i.e., a disk with an inner dust hole larger than the dust sublimation radius) on the basis of its SED, which is basically photospheric up to 8–10 μm and then rises at longer wavelengths (see Fig. 6). The subsequent spectroscopic follow-up with *Spitzer*/IRS revealed 10 and 20 μm silicate features and longer-wavelength crystalline features in the spectrum of Hn 24, though no polycyclic aromatic hydrocarbons (PAHs). Merín et al. (2010) also classified the object as a non-accretor on the basis of the 10% width of the Hα line (i.e., Natta et al. 2004) and estimated a very low disk mass (~5×10^{-5} $M_{\odot}$) from SED modeling. All these hints pointed toward an evolved disk around Hn 24. However, on the basis of the SED modeling with RADMC (Dullemond & Dominik 2004) and the model grid by Robitaille et al. (2006), Merín et al. (2010) concluded that Hn 24 does not show a significant inner hole.

Our SED modeling with RADMC-2D confirms this result. Models with inner radii larger than 0.5 AU have a low Bayesian probability to reproduce the SED of Hn 24 and the probability distribution peaks at $R_{\rm in} \approx 0.1$ AU. Merín et al. (2010) estimated an inclination angle around 65 deg for this object, consistent with our modeling, which shows that angles larger than 40 deg have a slightly higher probability to reproduce the SED (Figs. 7–8). Our disk mass estimate (>0.0001 $M_{\odot}$) also agrees with the mass inferred in Merín et al. (2010).

6. Summary and conclusions

We used PACS and SPIRE observations of Cha II performed within the frame of the HGBS key project, complemented by optical/IR imaging and spectroscopy available from the literature, to investigate the properties of the Class I to III YSOs in this star-forming region.

We detected 29 out of the 63 known YSOs in Cha II in at least one of the PACS/SPIRE pass-bands: 3 Class I YSOs (i.e., 100%), 1 flat source (i.e., 50%), 21 Class II objects (i.e., 55%), 3 Class III object (i.e., 16%) and the far-IR source IRAS 12522-7640, not classified because of the lack of near-IR data.

The PACS/SPIRE colors of YSOs are typically confined to the following ranges, where contamination by other field sources is expected to be low: $-0.7 \lesssim \log(F_{70}/F_{160}) \lesssim 0.5$, $-0.5 \lesssim \log(F_{160}/F_{250}) \lesssim 0.6$, $0.05 \lesssim \log(F_{250}/F_{350}) \lesssim 0.25$ and $-0.1 \lesssim \log(F_{350}/F_{500}) \lesssim 0.5$. When applied together, these four color conditions provide a reliable YSO selection tool.

For 26 YSOs in our sample, we modeled the SED using the RADMC-2D radiative transfer code and analyzed the resulting disk parameter values with a Bayesian method. We confirm that the Cha II YSOs present typical disk inner radii $\lesssim$0.1 AU and, thanks to the new *Herschel* data, we put reliable constraints on the on the lower limits to the mass and characteristic radius of these disks; we also attempted, for the first time, to estimate their flaring level. The lower limits to the characteristic radius are typically around 50 AU, although with a large spread, and the lower limits to the disk mass are proportional to the stellar masses with a typical 0.3% ratio. The estimated flaring angles, although very uncertain, point toward very flat disks ($1 + \phi \lesssim 1.2$).

We compared our results with previous estimates in the literature for other samples of low-mass M-type YSOs. Our results provide more evidence that the disk-to-stellar mass ratio is approximately constant across a broad range of stellar masses and that disks around Class II low-mass stars are flatter than disks around coeval higher-mass Class II stars. This supports the idea that disk properties show a dependence on stellar properties. Together with recent studies indicating that the properties of the given star-forming environment (such as metallicity and presence of of strong UV radiation fields) may affect disk evolution (Spezzi et al. 2012; De Marchi et al. 2011a,b), our results stress the important unknowns that still subsist in our current theory of disk evolution and planet formation. This paper paves the way for future studies on these open questions using larger YSO samples detected with the HGBS in other star forming-regions, such as Cha I and Serpens.

Acknowledgements. PACS has been developed by a consortium of institutes led by MPE (Germany) and including UVIE (Austria); KU Leuven, CSL, IMEC (Belgium); CEA, LAM (France); MPIA (Germany); INAF-IFSI/OAA/OAP/OAT, LENS, SISSA (Italy); IAC (Spain). This development has been supported by the funding agencies BMVIT (Austria), ESA-PRODEX (Belgium), CEA/CNES (France), DLR (Germany), ASI/INAF (Italy), and CICYT/MCYT (Spain). SPIRE has been developed by a consortium of institutes led by Cardiff University (UK) and including Univ. Lethbridge (Canada); NAOC (China); CEA, LAM (France); IFSI, Univ. Padua (Italy); IAC (Spain); Stockholm Observatory (Sweden); Imperial College London, RAL, UCL-MSSL, UKATC, Univ. Sussex (UK); and Caltech, JPL, NHSC, Univ. Colorado (USA). This development has been supported by national funding agencies: CSA (Canada); NAOC (China); CEA, CNES, CNRS (France); ASI (Italy); MCINN (Spain); SNSB (Sweden); STFC (UK); and NASA (USA). We are grateful to Juan M. Alcalá for providing the spectral type estimate of IRAS 12500-7658. We thank Kees Dullemond for the many explanations on typical parameter ranges for disk around T Tauri stars and the use of RADMC, and Daniel Dale, Luca Cortese and Margherita Bonzini for useful discussions on PACS/SPIRE colors of extragalactic sources. We are grateful to an anonymous referee, whose suggestions have helped us to improve the presentation of this work. N.L.J.C. and P.R. acknowledge support from the Belgian Federal Science Policy Office via the PRODEX Programme of ESA. This research has made use of the SIMBAD database, operated at CDS (Strasbourg, France) and data products from the Wide-field Infrared Survey Explorer (WISE), which is a joint project of the University of California, Los Angeles, and the Jet Propulsion Laboratory/California Institute of Technology, funded by the National Aeronautics and Space Administration

References

Ali, B., Tobin, J. J., Fischer, W. J., et al. 2010, A&A, 518, L119
Alcalá, J.M., Spezzi, L., Chapman, N., et al. 2008, ApJ, 676, 427
Allard, F., Hauschildt, P. H., & Schwenke, D. 2000, ApJ, 540, 1005
Amblard, A. Cooray, A., Serra, P., et al. 2010, A&A, 518, L9
André, P., Men'shchikov, A., Bontemps, S., et al. 2010, A&A, 518, L102
Andrews, S. M., & Williams, J. P. 2005, ApJ, 631, 1134
Apai, D., Pascucci, I., Henning, T., et al. 2002, ApJ, 573, L115
Apai, D., Pascucci, I., Bouwman, J., et al. 2005, Science, 310, 834
Biazzo, K., Alcalá, J. M., Covino, E., et al. 2012, A&A, 547, A104
Bressert, E., Testi, L., et al. 2013, A&A, submitted
Carpenter, J. M., Mamajek, E. E., Hillenbrand, L. A., & Meyer, M. R. 2006, ApJ, 651, L49
Chiang, E. I., & Goldreich, P. 1997, ApJ, 490, 368
Chiang, E. I., & Goldreich, P. 1999, ApJ, 519, 279
Cieza, L. A., Schreiber, M. R., Romero, G. A., et al. 2010, ApJ, 712, 925
Cieza, L. A., Olofsson, J., Harvey, P. M., et al. 2011, ApJ, 741, 25
Corbelli, E., Bianchi, S., Cortese, L., et al. 2012, A&A, 542, A32
D'Alessio, P., Canto, J., Calvet, N., & Lizano, S. 1998, ApJ, 500, 411
D'Alessio, P., Calvet, N., Hartmann, L., Lizano, S., & Cantó, J. 1999, ApJ, 527, 893
D'Alessio, P., Merin, B., Calvet, N., et al. 2005, Rev. Mex. Astron. Astrophys., 41, 61
Dale, D. A., Aniano, G., Engelbracht, C. W., et al. 2012, ApJ, 745, 95
De Marchi, G., Paresce, F., Panagia, N., et al. 2011a, ApJ, 739, 27
De Marchi, G., Panagia, N., Romaniello, M., et al. 2011b, ApJ, 740, 11
Dullemond, C. P., & Dominik, C. 2004, A&A, 417, 159
Dullemond, C. P., Dominik, C., & Natta, A. 2001, ApJ, 560, 957
Dullemond, C. P., van Zadelhoff, G. J., & Natta, A. 2002, A&A, 389, 464
Dunham, M. M., Arce, H. G., Allen, L. E., et al. 2013, AJ, 145, 94
Duschl, W. J., Gail, H.-P., & Tscharnuter, W. M. 1996, A&A, 312, 624
Dutrey, A., Lecavelier Des Etangs, A., & Augereau, J.-C. 2004, Comets II, 81
Evans, N. J. 2007, Final Delivery of Data from the c2d Legacy Project: IRAC and MIPS (Pasadena: SSC)
Evans, N. J., II, Allen, L. E., Blake, G. A., et al. 2003, PASP, 115, 965
Evans, N. J., II, Dunham, M. M., Jørgensen, J. K., et al. 2009, ApJS, 181, 321
Feigelson, E. D., & Montmerle, T. 1999, ARA&A, 37, 363
Greene, T. P., Wilking, B. A., Andre, P., Young, E. T., & Lada, C. J. 1994, ApJ, 434, 614
Griffin, M. J., Abergel, A., Abreu, A., et al. 2010, A&A, 518, L3
Hartmann, L., Megeath, S. T., Allen, L., et al. 2005, ApJ, 629, 881
Harvey, P., Merín, B., Huard, T. L., et al. 2007, ApJ, 663, 1149
Harvey, P. M., Henning, T., Ménard, F., et al. 2012a, ApJ, 744, L1
Harvey, P. M., Henning, T., Liu, Y., et al. 2012b, ApJ, 755, 6
Hatchell, J., Terebey, S., Huard, T., et al. 2012, ApJ, 754, 104
Hatziminaoglou, E., Omont A., Stevens, J.A., et al. 2010, A&A, 518, L33
Hauschildt, P. H., Allard, F., & Baron, E. 1999, ApJ, 512, 377
Kelly, B. C. 2007, ApJ, 665, 1489
Klein, R., Apai, D., Pascucci, I., Henning, T., & Waters, L. B. F. M. 2003, ApJ, 593, L57
Kornet, K., Wolf, S., & Różyczka, M. 2006, A&A, 458, 661
Lada, C. J., & Wilking, B. A. 1984, ApJ, 287, 610
Lada, C. J., Muench, A. A., Luhman, K. L., et al. 2006, AJ, 131, 1574
Lehtinen, K., Mattila, K., & Lemke, D. 2005, A&A, 437, 159
Lommen, D., Wright, C. M., Maddison, S. T., et al. 2007, A&A, 462, 211
Lommen, D., Jørgensen, J. K., van Dishoeck, E. F., & Crapsi, A. 2008, A&A, 481, 141
Lonsdale, C. J., Smith, H. E., Rowan-Robinson, M., et al. 2003, PASP, 115, 897
Luhman, K. L. 2008, Handbook of Star Forming Regions, II, 169
Lutz, D. 2010, PACS photometer point spread function (PACS document PICC-ME-TN-033)
Men'shchikov, A., André, P., Didelon, P., et al. 2012, A&A, 542, A81
Merín, B., Brown, J. M., Oliveira, I., et al. 2010, ApJ, 718, 1200
Metropolis, N., Rosenbluth, A. W., Rosenbluth, M. N., Teller, A. H., & Teller, E. 1953, J. Chem. Phys., 21, 1087
Molinari, S., Schisano, E., Faustini, F., et al. 2011, A&A, 530, A133
Muzerolle, J., Luhman, K. L., Briceño, C., Hartmann, L., & Calvet, N. 2005, ApJ, 625, 906
Muzerolle, J., Allen, L. E., Megeath, S. T., Hernández, J., & Gutermuth, R. A. 2010, ApJ, 708, 1107
Natta, A., Testi, L., Muzerolle, J., et al. 2004, A&A, 424, 603
Oliveira, I., Merín, B., Pontoppidan, K. M., et al. 2009, ApJ, 691, 672
Ott, S. 2010, Astronomical Data Analysis Software and Systems XIX, 434, 139
Pascucci, I., & Tachibana, S. 2010, in Protoplanetary Dust: Astrophysical and Cosmochemical Perspectives (CUP), 263
Pascucci, I., Apai, D., Henning, T., & Dullemond, C. P. 2003, ApJ, 590, L111
Pascucci, I., Apai, D., Luhman, K., et al. 2009, ApJ, 696, 143
Peterson, D. E., Caratti o Garatti, A., Bourke, T. L., et al. 2011, ApJS, 194, 43
Pilbratt, G. L., Riedinger, J. R., Passvogel, T., et al. 2010, A&A, 518, L1
Pinte, C., Padgett, D. L., Ménard, F., et al. 2008, A&A, 489, 633
Poglitsch, A., Waelkens, C., Geis, N., et al. 2010, A&A, 518, L2
Pollack, J. B., Hollenbach, D., Beckwith, S., et al. 1994, ApJ, 421, 615
Ribas, A., Merín, B., Bouy, H., et al. 2013, A&A, 552, A115
Ricci, L., Testi, L., Natta, A., et al. 2010, A&A, 512, A15
Ricci, L., Isella, A., Carpenter, J. M., & Testi, L. 2013, ApJ, 764, L27
Robitaille, T. P. 2011, A&A, 536, A79
Robitaille, T. P., Whitney, B. A., Indebetouw, R., Wood, K., & Denzmore, P. 2006, ApJS, 167, 256
Robitaille, T. P., Whitney, B. A., Indebetouw, R., & Wood, K. 2007, ApJS, 169, 328
Robitaille T. P., et al. 2012, Proc. Conf, The labyrinth of star formation, Crete 18−22 June, in press
Rodmann, J., Henning, T., Chandler, C. J., Mundy, L. G., & Wilner, D. J. 2006, A&A, 446, 211
Roussel, H. 2012 [arXiv:1205.2576]
Scholz, A., Jayawardhana, R., & Wood, K. 2006, ApJ, 645, 1498
Spezzi, L., Alcalá, J. M., Frasca, A., Covino, E., & Gandolfi, D. 2007, A&A, 470, 281
Spezzi, L., Alcalá, J. M., Covino, E., et al. 2008, ApJ, 680, 1295
Spezzi, L., Vernazza, P., Merín, B., et al. 2011, ApJ, 730, 65
Spezzi, L., de Marchi, G., Panagia, N., Sicilia-Aguilar, A., & Ercolano, B. 2012, MNRAS, 421, 78
Szűcs, L., Apai, D., Pascucci, I., & Dullemond, C. P. 2010, ApJ, 720, 1668
Ubach, C., Maddison, S. T., Wright, C. M., et al. 2012, MNRAS, 425, 3137
Walker, C., Wood, K., Lada, C. J., et al. 2004, MNRAS, 351, 607
Warren, S. G. 1984, Appl. Opt., 23, 1206
Weingartner, J. C., & Draine, B. T. 2001, ApJ, 548, 296
Whittet, D. C. B., Prusti, T., Franco, G. A. P., et al. 1997, A&A, 327, 1194
Williams, J. P., & Cieza, L. A. 2011, ARA&A, 49, 67
Winston, E., Cox, N. L. J., Prusti, T., et al. 2012, A&A, 545, A145
Wood, K., 2008, New Astron. Rev., 52, 145
Wright, E. L., Eisenhardt, P. R. M., Mainzer, A. K., et al. 2010, AJ, 140, 1868
Zubko, V. G., Mennella, V., Colangeli, L., & Bussoletti, E. 1996, MNRAS, 282, 1321

Pages 16 to 17 are available in the electronic edition of the journal at http://www.aanda.org

Table 2. *Herschel* PACS (70 to 160 μm) and SPIRE (250 to 500 μm) fluxes for known YSOs in Cha II detected with the HGBS.

Main Designation	Spectral Type[†]	Lada Class[‡]	RA(J2000)[⋆] (hh:mm:ss)	Dec(J2000)[⋆] (dd:mm:ss)	Dist.[△] ($''$)	70 μm[♠] (Jy)	100 μm[♠] (Jy)	160 μm[♠] (Jy)	250 μm[♠] (Jy)	350 μm[♠] (Jy)	500 μm[♠] (Jy)
IRAS 12416-7703	M2.5	II	12:45:07.85	–77:20:12.29	4.8	0.18 ± 0.02	OOF[II]	<9.00	<0.02	<0.13	<0.15
IRAS 12496-7650	F0	II	12:53:17.12	–77:07:10.86	0.3	100.80 ± 0.19	79.21 ± 0.20	46.16 ± 0.59	24.84 ± 0.38	15.14 ± 0.62	11.82 ± 0.32
IRAS 12500-7658	K5[♣]	I	12:53:42.83	–77:15:11.78	0.2	2.17 ± 0.03	2.44 ± 0.02	2.07 ± 0.05	1.50 ± 0.06	0.98 ± 0.07	0.49 ± 0.13
IRAS 12522-7640	–	–	12:55:50.06	–76:56:10.03	10.8	1.00 ± 0.04	0.84 ± 0.05	0.81 ± 0.10	0.98 ± 0.19	0.93 ± 0.20	0.48 ± 0.08
IRAS 12535-7623	M0	II	12:57:11.96	–76:40:10.02	1.6	0.20 ± 0.02	0.13 ± 0.01	0.13 ± 0.03	0.07 ± 0.06	<0.04	<0.02
WFI J12585611-7630105	M5	III	12:58:55.62	–76:30:10.77	1.7	0.15 ± 0.02	0.14 ± 0.01	0.05 ± 0.03	0.06 ± 0.03	<0.03	<0.03
ISO-CHAII 28	K4.3	I	12:59:06.68	–77:07:40.41	0.5	8.23 ± 0.04	6.69 ± 0.03	5.31 ± 0.10	11.71 ± 0.30	14.10 ± 0.58	33.70 ± 0.49
C 41	M5.5	F	12:59:11.39	–76:51:02.91	5.3	0.17 ± 0.02	0.11 ± 0.02	0.44 ± 0.06	0.13 ± 0.07	0.07 ± 0.06	<0.03
Sz 49	M0.5	II	13:00:53.51	–76:54:14.32	1.1	0.04 ± 0.03	0.18 ± 0.01	0.15 ± 0.03	0.14 ± 0.02	0.11 ± 0.03	0.07 ± 0.03
Sz 50	M3	II	13:00:55.46	–77:10:23.25	1.4	0.59 ± 0.02	0.55 ± 0.02	0.31 ± 0.07	<0.15	<0.03	<0.01
RX J1301.0-7654a	K5	III	13:00:56.56	–76:54:04.45	2.9	0.02 ± 0.01	0.01 ± 0.00	<0.14	<0.03	<0.03	<0.02
IRASF 12571-7657	K3	II	13:00:59.60	–77:14:02.95	1.3	0.38 ± 0.02	0.31 ± 0.02	0.24 ± 0.05	<0.10	<0.06	<0.03
Sz 51	K8.5	II	13:01:58.33	–77:51:22.76	2.2	0.15 ± 0.02	0.10 ± 0.01	0.29 ± 0.06	0.04 ± 0.02	<0.02	<0.02
CM Cha	K7	II	13:02:13.71	–76:37:57.11	0.9	0.58 ± 0.03	0.46 ± 0.03	0.43 ± 0.02	0.43 ± 0.02	0.38 ± 0.01	0.26 ± 0.01
IRAS 12589-7646	M4	III	13:02:50.60	–77:02:47.46	9.7	<0.03	1.73 ± 0.00	0.08 ± 0.03	<0.02	<0.02	<0.02
Hn 22	M2	II	13:04:23.57	–76:50:04.27	3.1	0.39 ± 0.03	0.39 ± 0.02	<0.48	<0.37	<0.28	<0.19
Hn 23	K5	II	13:04:23.94	–76:50:03.85	2.5	0.38 ± 0.02	0.35 ± 0.03	<0.48	<0.37	<0.28	<0.19
Sz 52	M2.5	II	13:04:24.93	–77:52:31.46	1.4	<0.18	0.04 ± 0.02	<0.90	<0.09	<0.06	<0.10
Hn 24	M0	II	13:04:55.94	–77:39:50.41	1.4	0.28 ± 0.02	0.25 ± 0.01	0.25 ± 0.07	<0.15	<0.09	<0.01
Hn 25	M2.5	II	13:05:08.47	–77:33:42.58	0.1	0.22 ± 0.02	0.23 ± 0.01	0.19 ± 0.03	0.13 ± 0.06	<0.02	<0.01
Sz 53	M1	II	13:05:12.68	–77:30:52.68	0.1	0.20 ± 0.02	0.15 ± 0.02	0.03 ± 0.03	0.07 ± 0.04	<0.04	<0.01
Sz 54	K5	II	13:05:20.99	–77:39:00.91	0.8	0.34 ± 0.02	0.28 ± 0.02	0.24 ± 0.07	<0.10	<0.03	<0.01
STc2d J130529.0-774140	–	II	13:05:27.08	–77:41:21.51	14.6	<0.43	0.04 ± 0.02	<0.31	<0.16	<0.24	<0.30
Sz 56	M4	II	13:06:38.69	–77:30:34.47	0.9	0.04 ± 0.01	0.02 ± 0.00	<0.02	<0.06	<0.06	<0.05
Sz 58	K5	II	13:06:57.29	–77:23:41.16	0.4	0.77 ± 0.02	0.91 ± 0.02	1.01 ± 0.05	0.83 ± 0.09	0.67 ± 0.11	0.43 ± 0.11
Sz 59	K7	II	13:07:09.10	–77:30:30.38	0.4	0.25 ± 0.02	0.32 ± 0.01	0.16 ± 0.03	0.11 ± 0.03	<0.04	<0.04
IRAS 13036-7644	–	I[◇]	13:07:37.02	–77:00:26.17	6.1	8.11 ± 0.06	OOF[II]	9.83 ± 0.64	32.77 ± 0.49	30.93 ± 0.43	19.72 ± 0.24
Sz 61	K5	II	13:08:06.41	–77:55:05.37	0.4	0.46 ± 0.03	0.45 ± 0.02	0.49 ± 0.03	0.45 ± 0.03	0.46 ± 0.03	0.41 ± 0.08
Sz 63	M3	II	13:10:04.32	–77:10:43.99	0.9	0.21 ± 0.02	OOF[II]	0.36 ± 0.02	0.25 ± 0.01	0.19 ± 0.01	0.13 ± 0.01

Notes. [(†)] From Spezzi et al. (2008). [(‡)] From Alcalá et al. (2008). [(⋆)] Coordinates are taken from the PACS-70 μm map. For IRAS 12589-7646, Sz 52, and STc2d J130529.0-774140 coordinates from the PACS-100 μm map are reported. [(△)] Angular distance between the HGBS coordinates and the coordinates reported in Spezzi et al. (2008) and Alcalá et al. (2008). [(♠)] The reported uncertainties are flux-extraction errors from *getsources*. The absolute calibration errors for PACS and SPIRE are 5% and 7%, respectively (see PACS and SPIRE observer manuals). [(♣)] Estimated by Alcalá (priv. comm.). [(◇)] From Lehtinen et al. (2005). [(II)] Out of field (see Sect. 2) .

Table 3. Flux upper limits for known YSOs in Cha II not detected with the HGBS.

Main Designation	Spectral Type[†]	Lada Class[†]	RA J2000[⋆] (hh:mm:ss)	Dec J2000[⋆] (dd:mm:ss)	70 μm (Jy)	100 μm (Jy)	160 μm (Jy)	250 μm (Jy)	350 μm (Jy)	500 μm (Jy)
IRAS 12448-7650	M0.5	III	12:48:25.70	–77:06:36.72	<0.04	<0.03	<0.03	<0.04	<0.04	<0.03
IRASF 12488-7658	M5.5	III	12:52:30.49	–77:15:12.92	<0.01	<0.01	<0.01	<0.05	<0.05	<0.04
WFI J12533662-7706393	M6	III	12:53:36.62	–77:06:39.31	<0.01	<0.07	<0.07	<0.19	<0.23	<0.34
C 17	M1.5	III	12:53:38.84	–77:15:53.21	<0.01	<0.01	<0.07	<0.07	<0.10	<0.10
C 33	M1	III	12:55:25.72	–77:00:46.62	<0.01	<0.01	<0.08	<0.10	<0.12	<0.14
Sz 46N	M1	II	12:56:33.59	–76:45:45.18	<0.08	<0.01	<0.18	<0.05	<0.04	<0.03
Sz 47	–	III	12:56:58.63	–76:47:06.72	<0.00	<0.00	<0.00	<0.06	<0.08	<0.08
SSTc2d J125758.7-770120	M9	II	12:57:58.70	–77:01:19.50	<0.02	<0.02	<0.05	<0.04	<0.05	<0.04
ISO-CHAII 13	M7	II	12:58:06.67	–77:09:09.22	<0.07	<0.10	<0.10	<0.25	<0.28	<0.20
WFI J12583675-7704065	M9	III	12:58:36.75	–77:04:06.53	<0.00	<0.02	<0.01	<0.05	<0.07	<0.10
ISO-CHAII 29	M0	III	12:59:10.19	–77:12:13.72	<0.05	<0.09	<0.59[♣]	<1.34[♣]	<2.24[♣]	<2.65[♣]
IRAS 12556-7731	M5	III	12:59:26.50	–77:47:08.70	<0.90	<0.36	<0.05	<0.16	<0.15	<0.09
WFI J13005297-7709478	M9	III	13:00:52.97	–77:09:47.77	<0.10	<0.03	<0.20	<0.20	<0.20	<0.30
Sz 48NE[‡]	M0.5	II	13:00:53.15	–77:09:09.18	<0.02	<0.03	<0.07	<0.23	<0.31	<0.28
Sz 48SW[‡]	M1	II	13:00:53.56	–77:09:08.28	<0.02	<0.03	<0.07	<0.23	<0.31	<0.28
WFI J13005531-7708295	M2.5	III	13:00:55.31	–77:08:29.54	<0.00	<0.00	<0.00	<0.19	<0.27	<0.57
C 50	M5	II	13:02:22.82	–77:34:49.51	<0.00	<0.00	<0.03	<0.09	<0.10	<0.10
RX J1303.1-7706	M0	III	13:03:04.46	–77:07:02.75	<0.02	<0.01	<0.01	<0.02	<0.02	<0.03
C 51	M4.5	III	13:03:09.04	–77:55:59.52	<0.01	<0.01	<0.01	<0.05	<0.06	<0.06
WFI J13031615-7629381	M7	III	13:03:16.15	–76:29:38.15	<0.00	OOF[II]	<0.01	<0.01	<0.04	<0.01
SSTc2d J130521.7-773810	C	F	13:05:21.66	–77:38:10.14	<0.02	<0.01	<0.01	<0.02	<0.02	<0.20
SSTc2d J130540.8-773958	L1	II	13:05:40.80	–77:39:58.20	<0.00	<0.01	<0.01	<0.16	<0.22	<0.29
Sz 55	M2	II	13:06:30.49	–77:34:00.12	<0.02	<0.05	<0.01	<0.04	<0.03	<0.08
Sz 57	M5	II	13:06:56.56	–77:23:09.46	<0.05	<0.90	<0.14	<0.03	<0.04	<0.04
C 62	M4.5	II	13:07:18.04	–77:40:53.00	<0.04	<0.02	<0.01	<0.12	<0.20	<0.19
Sz 60W[‡]	M1	III	13:07:22.30	–77:37:22.62	<0.04	<0.06	<0.06	<0.03	<0.02	<0.02
Sz 60E[‡]	M4	II	13:07:23.33	–77:37:23.20	<0.04	<0.06	<0.06	<0.03	<0.02	<0.02
Hn 26	M2	II	13:07:48.50	–77:41:21.73	<0.02	<0.05	<0.13	<0.09	<0.12	<0.13
C 66	M4.5	II	13:08:27.19	–77:43:23.41	<0.03	<0.03	<0.10	<0.13	<0.48	<0.66
IRASF 13052-7653NW[‡]	M0.5	II	13:09:09.81	–77:09:43.52	<0.04	OOF[II]	<0.07	<0.02	<0.01	<0.02
IRASF 13052-7653N[‡]	M1.5	II	13:09:10.98	–77:09:44.14	<0.04	OOF[II]	<0.07	<0.02	<0.01	<0.02
Sz 62	M2.5	II	13:09:50.44	–77:57:23.94	<0.02	<0.06	<0.08	<0.06	<0.05	<0.03
2MASS 13125238-7739182	M4.5	III	13:12:52.37	–77:39:18.58	<0.03	OOF[II]	<0.01	<0.01	<0.01	<0.01
Sz 64	M5	II	13:14:03.83	–77:53:07.48	<0.03	<0.03	<0.10	<0.03	<0.03	<0.03

Notes. [(†)] Spectral types and Lada classes are taken from Spezzi et al. (2008) and Alcalá et al. (2008), respectively. [(⋆)] Coordinates are taken from the optical survey in Spezzi et al. (2008). [(♣)] The object is located in a region with strong background emission. [(‡)] Binary system (Spezzi et al. 2008). [(II)] Out of field (see Sect. 2).